Astronomy & Astrophysics

The GAPS programme at TNG

XXIV. An eccentric Neptune-mass planet near the inner edge of the BD-11 4672 habitable zone[*]

D. Barbato[1,2,3], M. Pinamonti[2], A. Sozzetti[2], K. Biazzo[4,5], S. Benatti[6], M. Damasso[2], S. Desidera[7], A. F. Lanza[4], J. Maldonado[6], L. Mancini[8,9,2], G. Scandariato[4], L. Affer[6], G. Andreuzzi[10,5], A. Bignamini[11], A. S. Bonomo[2], F. Borsa[12], I. Carleo[13,7], R. Claudi[7], R. Cosentino[10], E. Covino[14], A. F. M. Fiorenzano[10], P. Giacobbe[2], A. Harutyunyan[10], C. Knapic[11], G. Leto[4], V. Lorenzi[10,15], A. Maggio[6], L. Malavolta[4], G. Micela[6], E. Molinari[16], M. Molinaro[11], V. Nascimbeni[7], I. Pagano[4], M. Pedani[10], G. Piotto[17], E. Poretti[10,12], and M. Rainer[18]

(Affiliations can be found after the references)

ABSTRACT

Context. With the growth of comparative exoplanetology, it is becoming increasingly clear that investigating the relationships between inner and outer planets plays a key role in discriminating between competing formation and evolution models. To do so, it is important to probe the inner region of systems that host long-period giants in search of undetected lower-mass planetary companions.

Aims. In this work, we present our results on the K-dwarf star BD-11 4672, which is already known to host a long-period giant planet, as the first output of a subsample of the GAPS programme specifically aimed at assessing the impact of inefficient migration of planets formed beyond the snowline by searching for Neptune-mass and super-Earth planetary companions of known longer-period giants.

Methods. We used the high-precision HARPS-N observations of BD-11 4672 in conjunction with time series taken from the literature in order to search for additional inner planetary signals to be fitted using differential evolution Markov chain Monte Carlo. The long-term stability of the new orbital solutions was tested with N-body dynamical simulations.

Results. We report the detection of BD-11 4672 c, a new Neptune-mass planet with an orbital period of $74.20^{+0.06}_{-0.08}$ d, eccentricity of $0.40^{+0.13}_{-0.15}$, semimajor axis of 0.30 ± 0.01 au, and minimum mass $15.37^{+2.97}_{-2.81}$ $M_\oplus$, orbiting slightly outside the inner edge of the optimistic circumstellar habitable zone. In order to assess its impact on the dynamical stability of the habitable zone, we computed the angular momentum deficit of the system, showing that planet c has a severe negative impact on the stability of possible additional lower-mass temperate planets. The BD-11 4672 system is notable for its architecture, hosting both a long-period giant planet and an inner lower-mass planet, the latter being one of the most eccentric Neptune-mass planets known at similar periods.

Key words. stars: individual: BD-11 4672 – techniques: radial velocities – planetary systems – planets and satellites: detection – planets and satellites: dynamical evolution and stability

1. Introduction

The large number and variety of exoplanetary systems that are known so far has enabled the field of comparative exoplanetology to thrive, producing, in recent years, a number of studies that focus on planetary mass distributions and system architecture, as well as their dependences on the characteristics of their host stars (e.g. Winn & Fabrycky 2015; Hobson & Gomez 2017; Johnson et al. 2010; Wittenmyer et al. 2020a). As the competing formation and migration models of both terrestrial and giant planets produce different outcomes in terms of orbits and mass hierarchy (Raymond et al. 2008; Cossou et al. 2014; Schlaufman 2014; Morbidelli & Raymond 2016; Izidoro et al. 2015a,b; Bitsch et al. 2015; Lambrechts et al. 2019), the study of the architecture of known exoplanetary systems is a key factor in supporting or disproving the current theoretical models.

In particular, the various formation and migration models of close-in super-Earths and Neptunes tend to predict different configurations of the inner regions of planetary systems in the presence of long-period giant planets. In the inward migration model, super-Earth embryos form in the outer protoplanetary disk and migrate inwards to become hot super-Earths or hot Neptunes; however, if the innermost embryo grows into a gas giant planet, it will block the inward migration of more distant cores (Izidoro et al. 2015a,b). This model, therefore, results in a lack of inner lower-mass planets in the presence of outer giant planets. If cold Jupiters are formed, instead, at larger orbital distances (Bitsch et al. 2015), any subgiant planets formed near the snowline are able to migrate inwardly and become hot Neptunes and super-Earths, resulting in the presence of both close-in lower-mass bodies and long-period giant planets.

Although the search for super-Earths or Neptune-mass planets on inner orbits in the presence of long-period giant planets is clearly fundamental in advancing our understanding of the dynamical history of planetary systems, technical and strategic issues have often severely impacted this endeavour. However, encouraging signs of our growing understanding in terms of the

---

[*] Based on observations made with the Italian Telescopio Nazionale *Galileo* (TNG) operated by the Fundación Galileo Galilei (FGG) of the Istituto Nazionale di Astrofisica (INAF) at the Observatorio del Roque de los Muchachos (La Palma, Canary Islands, Spain).

characterisation of the inner region of planetary systems have been provided by recent observational programmes and instrumentation that are well-suited for such an endeavour and also by the results of comparative exoplanetology. An analysis conducted in Zhu & Wu (2018) on inner super-Earths and Neptunes discovered by radial velocities and outer Jupiter analogs suggests that the majority of systems hosting cold Jupiters should also feature additional inner sub-Neptune planetary bodies. More recently, the 18 yr of observations collected by the Anglo-Australian Planet Search reported in Wittenmyer et al. (2020b) suggests that the occurrence rate of giant planets orbiting Solar-type stars with a semimajor axis $a > 1$ au is ~7%, about eight times higher than those on closer-in orbits. Such a predominance of long-period giant planet provides fertile ground for the search of additional lower-mass planets in the inner orbital region and the study of early formation and inward migration mechanisms. In a previous survey (Barbato et al. 2018), we monitored 20 Sun-like stars that are known to host long-period giant planets and derived an occurrence rate of inner lower-mass planets <10% for $M \sin i > 10 M_\oplus$. However, the completeness of our survey was negatively impacted by the fact that the average number of data points collected per star were lower than initially foreseen, severely limiting the sensitivity to lower-mass companions. Indeed, the real occurrence rate of such systems may actually be higher, as additional inner low-mass planets in the presence of outer giant planets could be detected with intensive sampling and longer observational timespans (e.g. Benatti et al. 2020).

In this context, K and M dwarf stars represent a fertile field for the search of inner super-Earths and Neptune-mass planetary companions. Such stars represent the most numerous stellar population in the Milky Way (e.g. Chabrier & Baraffe 2000; Winters et al. 2015) and their low mass, size, and temperature make them prime candidates for the search of planetary systems, easing the detection of signals produced by sub-Neptune planetary companions and hosting a variety of systems featuring super-Earths and Neptune-mass planets (Bonfils et al. 2012; Dressing & Charbonneau 2013; Crossfield et al. 2015; Astudillo-Defru et al. 2017b; Pinamonti et al. 2018). While it has been observed that dwarfs less massive than our Sun are less likely to host a giant planet (Butler et al. 2004; Johnson et al. 2007, 2010; Bonfils et al. 2013), as expected by theoretical studies (e.g. Laughlin et al. 2004; Mordasini et al. 2009a,b), the discovery of M-dwarfs hosting planetary systems featuring both giant planets and sub-Neptunians companions, such as the GJ 676 A system (Forveille et al. 2011; Anglada-Escudé & Tuomi 2012), which hosts two inner sub-Neptunian planets and two outer giant planets, suggests that the formation and survival of multiple planetary systems featuring a wide range of planetary masses is not completely suppressed around dwarf stars.

The observational programme Global Architecture of Planetary Systems (GAPS, see Covino et al. 2013; Desidera et al. 2013) is aimed at investigating the variety and origins of the architecture of exoplanetary systems with the High Accuracy Radial velocity Planet Searcher in the Northern hemisphere (HARPS-N, Cosentino et al. 2012) at the Telescopio Nazionale *Galileo* (TNG) in La Palma. Within this context, a subset of planet-hosting K and M dwarfs has been selected and observed over the last few years in order to search for inner super-Earths and Neptune-mass planetary companions to outer long-period giants and assessing the impact of inefficient migration of planets formed beyond the snowline of such dwarf stellar hosts.

In this paper, we present the first result of the GAPS observations on this stellar sample, namely the new characterisation of the planetary system orbiting the K-dwarf star BD-11 4672

(also known as GJ 717). Moutou et al. (2011) first reported hints of the presence of a planetary companion around BD-11 4672 following observations with the High Accuracy Radial velocity Planet Searcher (HARPS, Mayor et al. 2003) at the ESO La Silla 3.6 m telescope. Additional HARPS monitoring (Moutou et al. 2015) led to the detection of the planetary companion BD-11 4672 b, with a period of 1667^{+33}_{-31} days, and minimum mass of $M \sin i = 0.53 \pm 0.05 M_{\rm Jup}$.

In Sect. 2, we provide updates on the parameters of the stellar host. In Sect. 3, we provide an overview of the HARPS-N observations, analyse the stellar activity cycles, and fit our HARPS-N radial velocity measurements in conjunction with archival HARPS data. In Sect. 4, we assess the dynamical stability of the system, focusing on the circumstellar habitable zone before concluding and discussing the results of this work in Sect. 5.

2. Stellar parameters

In this section we present a new spectroscopic characterisation of the astrophysical properties of the host star BD-11 4672. We measured effective temperature $T_{\rm eff}$, surface gravity $\log g$, microturbulence velocity ξ and iron abundance [Fe/H], using a method based on line equivalent widths. The measurement of equivalent widths was done with the software IRAF (Tody 1993) from the coadded spectrum built from individual HARPS-N spectra used for the radial velocity measurements and described in Sect. 3. We then adopted the Castelli & Kurucz (2004) grid of model atmospheres and the spectral analysis package MOOG (Sneden 1973; 2017 version). The result for $T_{\rm eff}$ was derived by imposing that the abundance of Fe I is not dependent on the line excitation potentials, ξ by obtaining the independence between Fe I abundance and equivalent widths, and $\log g$ by the Fe I/Fe II ionisation equilibrium condition.

With this method, we obtain the following stellar parameters: $T_{\rm eff} = 4500 \pm 130$ K, $\log g = 4.5 \pm 0.2$, $\xi = 0.85 \pm 0.40$ km s^{-1}, and [Fe/H] $= -0.35 \pm 0.15$ dex. From these values of stellar parameters we followed the method detailed in Damasso et al. (2015) and Biazzo et al. (2015), and references therein, to measure other elemental abundances differentially with respect to the Sun (see Table 1). The first value of the uncertainty on elemental abundance is obtained from the equivalent widths measurements, while the second value is the root sum square of the errors due to the uncertainties in stellar parameters. With an iron abundance of [Fe/H] $= -0.35 \pm 0.15$ dex, we can consider the star BD-11 4672 as a metal-poor host star, although it is not as metal-poor as other planet-hosting stars we observed with HARPS-N within the GAPS programme (Barbato et al. 2019).

We also derived the projected rotational velocity $v \sin i$ through a spectral synthesis of two regions around 6200 and 6700 Å, as done in Barbato et al. (2019). Using the same grid of model atmospheres and code and by assuming a macroturbolence $v_{\rm macro} = 2.0$ km s^{-1} (Valenti & Fischer 2005), we find $v \sin i = 1.0 \pm 0.5$ km s^{-1}, which is below the HARPS-N spectral resolution, thus suggesting a slow stellar rotation, unless the star is observed nearly pole-on. Moutou et al. (2015) did not measure the projected rotation velocity, and the authors were only able to put an upper limit $v \sin i < 2$ km s^{-1}, which is consistent with our findings.

Considering the elemental abundances of the field stars listed in the catalogues by Soubiran & Girard (2005) and Adibekyan et al. (2012a), and applying the prescriptions reported in Biazzo et al. (2015), we can also investigate which stellar population BD-11 4672 belongs to. We thus considered the abundances of

Table 1. Elemental abundances for star BD-11 4672.

Elemental abundances (dex)	
[Fe I/H]	$-0.35 \pm 0.15 \, (+-0.06)$
[Fe II/H]	$-0.35 \pm 0.27 \, (+-0.24)$
[Na I/H]	$-0.37 \pm 0.03 \, (+-0.14)$
[Mg I/H]	$-0.48 \pm 0.19 \, (+-0.02)$
[Al I/H]	$-0.24 \pm 0.14 \, (+-0.08)$
[Si I/H]	$-0.39 \pm 0.16 \, (+-0.09)$
[Ca I/H]	$-0.17 \pm 0.06 \, (+-0.19)$
[Ti I/H]	$-0.18 \pm 0.08 \, (+-0.21)$
[Ti II/H]	$-0.61 \pm 0.06 \, (+-0.09)$
[Cr I/H]	$-0.27 \pm 0.11 \, (+-0.13)$
[Cr II/H]	$-0.30 \pm 0.08 \, (+-0.12)$
[Ni I/H]	$-0.49 \pm 0.18 \, (+-0.04)$
[Ba II/H]	$-0.43 \pm 0.07 \, (+-0.19)$
[C I/H]	$+0.24 \pm 0.03 \, (+-0.16)$
[Y II/H]	$-0.62 \pm 0.16 \, (+-0.09)$
[Eu II/H]	$+0.04 \pm 0.04 \, (+-0.07)$
[Nd II/H]	$-0.44 \pm 0.38 \, (+-0.09)$
[Nd II/H]	$+0.43 \pm 0.37 \, (+-0.13)$
[Zn I/H]	$+0.11 \pm 0.04 \, (+-0.12)$

Notes. The first errors refer to the measure of the equivalent width, while the errors in parentheses are obtained from the root sum square of the abundance error caused by uncertainties on T_{eff}, $\log g$, and ξ.
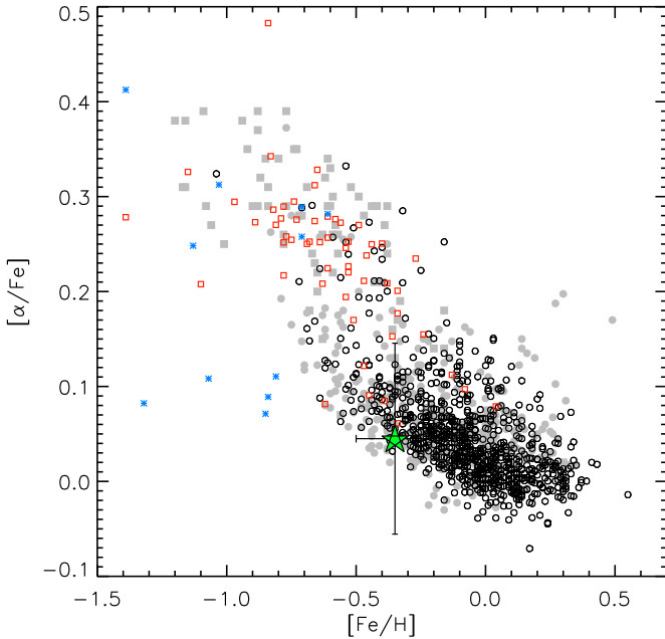

Fig. 1. [α/Fe] vs. [Fe/H] for BD-11 4672, identified here by the green star symbol. Thin-disc, thick-disc, and halo stars are shown with circles, squares, and asterisks, respectively (filled symbols: Soubiran & Girard 2005; open symbols: Adibekyan et al. 2012a).

the α-elements Mg, Si, Ca, and Ti. Figure 1 shows the position of BD-11 4672 in the [α/Fe] versus [Fe/H] diagram. Based on these chemical indicators, the star seems to be a member of the thin-disc population. Additionally, we can classify BD-11 4672 on the basis of its Galactic kinematics, using *Gaia* Data Release 2 proper motions (Gaia Collaboration 2018) to compute the thick-to-thin disc probability ratio TD/D defined in Bensby et al.

Table 2. Stellar parameters for BD-11 4672.

BD-11 4672 (GJ 717)	
α (J2000) [a]	$18^{\mathrm{h}}33^{\mathrm{m}}28.8^{\mathrm{s}}$
δ (J2000) [a]	$-11°38'9''$
π (mas) [a]	36.781 ± 0.046
μ_α (mas yr^{-1}) [a]	-288.590 ± 0.097
μ_δ (mas yr^{-1}) [a]	-235.560 ± 0.089
B (mag) [b]	11.21 ± 0.10
V (mag) [b]	9.99 ± 0.05
R (mag) [c]	9.60 ± 0.10
G (mag) [a]	9.4851 ± 0.0005
J (mag) [d]	7.651 ± 0.020
H (mag) [d]	7.031 ± 0.030
K (mag) [d]	6.867 ± 0.020
Spectral type [e]	K7V
$M_\star$ ($M_\odot$) [f]	$0.651^{+0.031}_{-0.029}$
$R_\star$ ($R_\odot$) [f]	$0.639^{+0.020}_{-0.022}$
$\rho_\star$ (g cm^{-3}) [f]	$3.53^{+0.34}_{-0.28}$
T_{eff} (K) [f]	4550 ± 110
$L_\star$ ($L_\odot$) [f]	$0.157^{+0.019}_{-0.017}$
$\log g$ (cgs) [f]	$4.642^{+0.027}_{-0.025}$
Age (Gyr) [f]	$7.4^{+4.5}_{-4.9}$
$\log R'_{\mathrm{HK}}$ [g]	-4.65
P_{rot} (d) [g]	~ 25

Notes. [a]Retrieved from *Gaia* Data Release 2 (Gaia Collaboration 2018), [b]retrieved from Høg et al. (2000), [c]retrieved from Zacharias et al. (2012), [d]retrieved from Cutri et al. (2003), [e]retrieved from Skiff (2014), [f]obtained from the SED fitting discussed in Sect. 2, [g]expected value obtained from the activity analysis discussed in Sect. 3.1

(2003). For BD-11 4672 we find $TD/D = 0.45$; while this value hints at an intermediate kinematics between the two populations, tests on different population normalisations conducted in Bensby et al. (2005) show that stars with $TD/D < 0.6$ can usually be safely regarded as thin disc stars. Both chemical composition and kinematics criteria therefore point towards BD-11 4672 as being a member of the thin-disc stellar population.

In order to provide updated estimates of all stellar parameters we fit the Spectral Energy Distribution (SED) via the MESA Isochrones and Stellar Tracks (MIST; Dotter 2016; Choi et al. 2016) through the EXOFASTv2 suite (Eastman et al. 2019). We fitted the available archival magnitudes listed in Table 2, imposing gaussian priors on T_{eff} and [Fe/H] as obtained by the ionisation equilibrium and on parallax π based on the *Gaia* DR2 astrometric measurement, after correcting the DR2 value for the systematic offset of $-82 \pm 33 \, \mu\mathrm{as}$ as reported in Stassun & Torres (2018); this astrometric prior helps in constraining the stellar radius and improves the precision of the stellar parameters resulting from the SED fitting procedure. The resulting stellar parameters, listed in Table 2, are generally comparable within 2σ to the stellar characterisation reported in Moutou et al. (2015), with the exception of the star's mass and radius, for which we find larger values which differ from those of Moutou et al. (2015) by 2.5σ and 4.3σ, respectively.

With these updated stellar parameters, we use the 1D radiative-convective, cloud-free climate model detailed in Kopparapu et al. (2013, 2014) to compute the inner and outer boundaries of the circumstellar habitable zone. Considering the

runaway and maximum greenhouse limits, we characterise the conservative habitable zone as spanning from 0.42 to 0.77 au. Using, instead, the recent Venus and early Mars limits, we find the optimistic habitable zone ranging from 0.33 to 0.81 au.

3. Spectroscopic time series and analyses

We observed BD-11 4672 with HARPS-N from May 2018 (BJD = 2 458 268.6) to September 2019 (BJD = 2 458 747.4), obtaining a total of 68 datapoints over a timespan of 479 days with a mean exposure time of 1100 s and a mean signal-to-noise ratio (S/N) of 66. The spectra collected were reduced using the HARPS-N data reduction software (DRS, Lovis & Pepe 2007), while the radial velocities extraction was performed with the template-enhanced radial velocity re-analysis application pipeline (TERRA, Anglada-Escudé & Butler 2012), which proved to provide more precise radial velocity measurements for late-type stars. The radial velocity time series obtained as a result exhibits a median radial velocity uncertainty of 0.95 m s^{-1} and a weighted root mean square (w.r.m.s.) of 7.23 m s^{-1}.

In the following analysis, we use our HARPS-N measurements in combination with the HARPS observations presented in Moutou et al. (2015), along with three additional HARPS archival data points collected from July 2014 to early May 2015, all of which we newly reduced using TERRA. While an additional archival HARPS datapoint at epoch 24557851.82 is available, it was collected after the late May 2015 optical fibre upgrade (Lo Curto et al. 2015), therefore introducing an instrumental offset depending on the stellar spectral type (Trifonov et al. 2020). Rather than treating this single data point as independent from the rest of the time series, we exclude this point from all analysis. The historical time series is then composed by 43 datapoints over a timespan of 3568 days with median error of 1.38 m s^{-1} and w.r.m.s. of 8.55 m s^{-1}.

Therefore, the full HARPS and HARPS-N time series we take into exam is composed of a total of 111 radial velocity measurements over 5170 days with a median uncertainty of 1.14 m s^{-1} and w.r.m.s. of 7.77 m s^{-1}. The complete lists of HARPS and HARPS-N radial velocity measurements, in addition to the time series of the stellar activity indicators discussed in Sect. 3.1, are shown in Tables A.1 and A.2.

In order to study the stellar activity as described in Sect. 3.1, we computed a series of activity indices for all the HARPS and HARPS-N spectra at our disposal to obtain consistent time series of indicators in order to better analyse the long-term evolution of the stellar activity. Following the procedure from Gomes da Silva et al. (2011), we derived the activity indices for the Ca II H&K, Hα, and Na I D$_1$ D$_2$ stellar spectral lines.

3.1. Activity

We studied the stellar activity of BD-114672, expanding the analyses from Moutou et al. (2011, 2015). The authors of those studies searched for correlations between the RVs and activity indices derived from the HARPS spectra and for signals of activity evolution on time scales comparable to the orbital period of BD-11 4672 b. Even though the results from Moutou et al. (2011) were generally inconclusive, Moutou et al. (2015) found no evidence of the 1667 d signal to be produced by a magnetic cycle.

First we checked for the presence of possible outliers in the activity indices time series, which can be caused by stellar flares or other transient phenomena. To do so, we identified the epochs for which any activity index deviated more than three standard
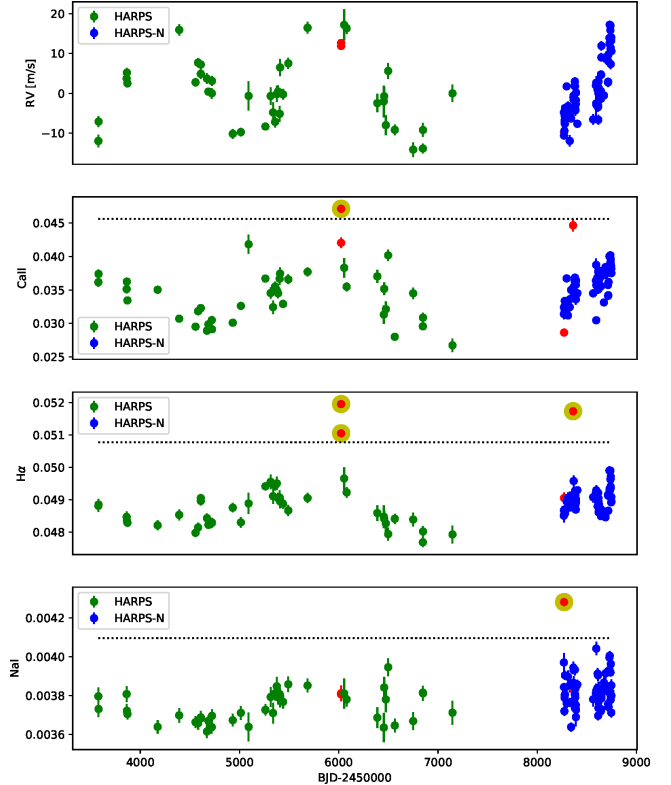

Fig. 2. Combined HARPS and HARPS-N time series of the RVs and activity indices of BD-11 4672. The red dots represent the outliers identified in the activity time series and the yellow shades mark the outliers identified in each time series. The dotted black lines indicates the threshold value of three standard deviations from the median.

deviations from the median of the respective time series. These observational epochs were discarded from all the activity, asymmetry, and RV time series in all the following analyses since the data could be affected by transient phenomena which are not considered by our models.

In the bottom three panels of Fig. 2 we show the time series for the activity indices, highlighting the four outliers identified with the aforementioned procedure (BJD = 2 456 023.85, 2 456 023.89, 2 458 270.69 and 2 458 361.38). There clearly appears to be some long-term modulation in the Ca II H&K, and Hα time series and, if less evident, in the Na I D$_1$ D$_2$. To study these potential signals we computed the Generalized Lomb Scargle periodogram (GLS, Zechmeister & Kürster 2009) of the activity time series. The results are shown in the top row of Fig. 3. The Ca II H&K and Na I D$_1$ D$_2$ periodograms are dominated by long-period signals, with similar periods of $P \simeq 3000$ d, while the Hα shows a significant peak around that period, but is dominated by a shorter periodicity.

Since also the RV time series, shown in the top panel of Fig. 2, presents a long-term periodicity, corresponding to the orbital period $P_b \simeq 1700$ d of BD-114672 b (Moutou et al. 2015), we studied the correlation between the RV and activity indices time series. We computed the Pearson correlation coefficients and found no significant correlation ($|\rho| < 0.3$) for any indices except Ca II H&K, which showed a moderate correlation $\rho_{Ca II} = 0.45$. As can be seen in Fig. 4, this correlation is dominated by the HARPS-N data, which cover only small fractions of the 3000 d periodicity dominating the activity time series and of the 1700 d orbital signal of BD-114672 b, in which both signals show an ascending trend: computing the Pearson correlation
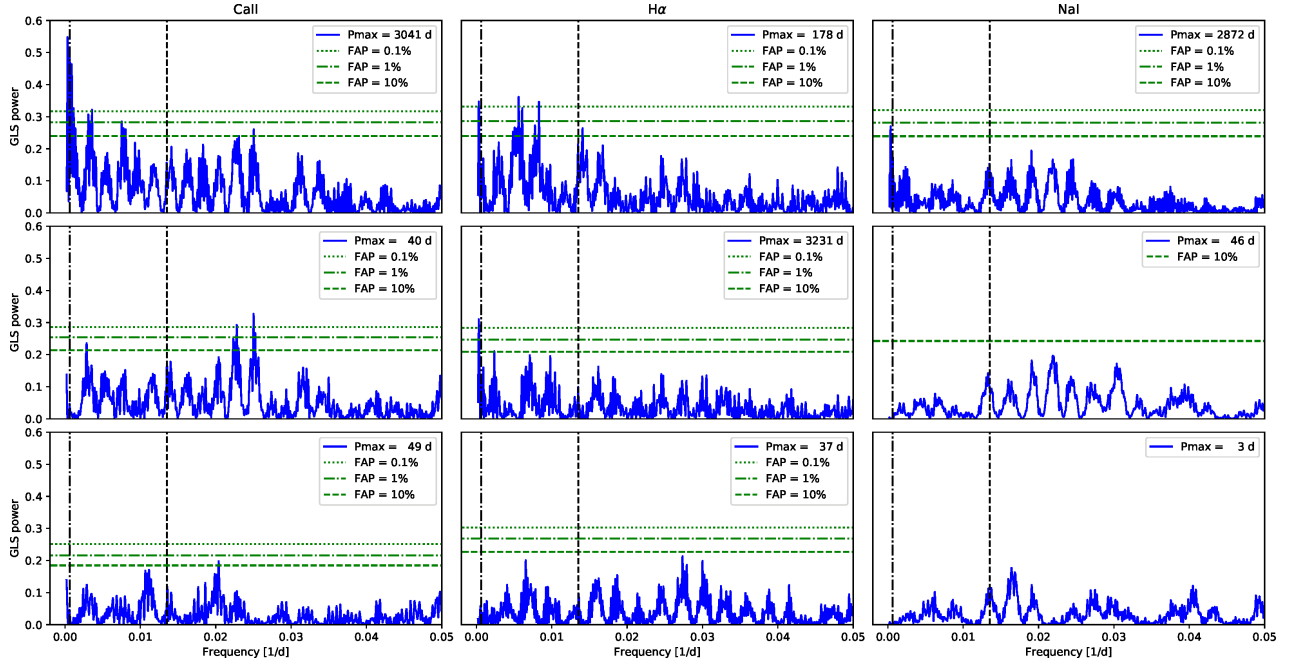
Fig. 3. Generalised Lomb-Scargle periodograms of the activity indices time series (*top row*) and residuals after pre-whitening (*middle and bottom rows*). The period value of the principal peak of each periodogram is noted in the legend as Pmax, and the dashed and dot-dashed black vertical lines indicates the signals discussed in Sect. 3.2. The horizontal green lines indicates the false alarm probability (FAP) levels, as indicated in the legend. The FAP levels are computed via 10 000-iterations bootstrap. In the residuals periodograms only the FAP levels less significant than the principal peak of the previous periodograms are marked.
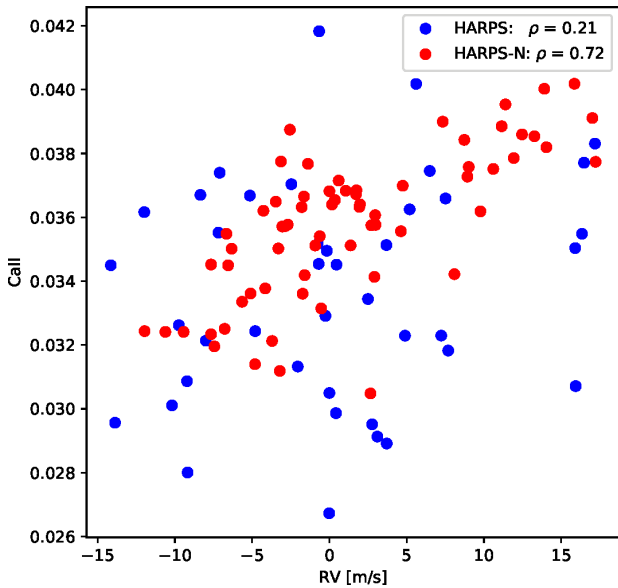

Fig. 4. Ca II H&K index time series as a function of the radial velocity measurements.

coefficient on the HARPS time series, which has a timespan longer than both the involved periods, the correlation drops to $\rho_{Ca\,II} = 0.21$. This suggests that the moderate value of $\rho_{Ca\,II}$ for the combined time series is merely an artefact of the uneven sampling of the periodic signals dominating the RV and activity data. Moreover, while performing the fits described in Sect. 3.2, we repeated the computation of the Pearson correlation coefficients with the activity indices on the RV residuals of the fitted models: no increase in the correlation was observed, thus confirming that the emerging signals shown in Fig. 5 are not activity-related.

Additional significant peaks can be seen in the top row of Fig. 3. We performed a residuals analysis of the activity time series after the subtraction of the dominant peak in each GLS periodogram. The results are shown in the middle and bottom rows of Fig. 3 for the analyses of the first and second residuals, respectively. We can see in the middle row that the Ca II H&K and Na I D_1 D_2 residuals both show signals around ~40 d, even if in the case of Na I D_1 D_2 the peak is not significant; in the Hα residuals, the 3000 d long period signals becomes dominant. Only the second residuals of the Ca II H&K show a significant signal, which is again close to 40 d. We thus have three dominant periodicities in the analysed activity indices: ~3000, ~200, and ~40 d. The longest periodicity, which is present in all three activity indicators, can be attributed to a solar-like activity cycle, since similar cycles spanning around 7–10 yr have been observed in other stars of similar spectral type (Boro Saikia et al. 2018).

We collected the available All Sky Automated Survey (ASAS, Pojmanski 1997) photometric timeseries for BD-11 4672, composed of 650 datapoints spanning over 3173 days from February 2001 to November 2009. We performed a GLS analysis of these data, and identified a dominant periodicity of ~3000 d, consistent with the long-period activity cycle we identify in the HARPS and HARPS-N activity indices. However, the relatively short timespan of the available ASAS photometry does not allow for a more precise characterisation of this long-term periodicity.

Regarding the shorter periodicities, Scandariato et al. (2017) notes that in cold and relatively inactive stars, periods around ~200 d are usually linked to the evolution timescale of active regions, and for the same stars rotation periods are typically around ~30−40 d. No information is present in the literature on the rotation period of BD-11 4672, which is usually linked to the dominant signals in the activity indicators. From the value of $v \sin i$ derived in Sect. 2, we can estimate the maximum rotation
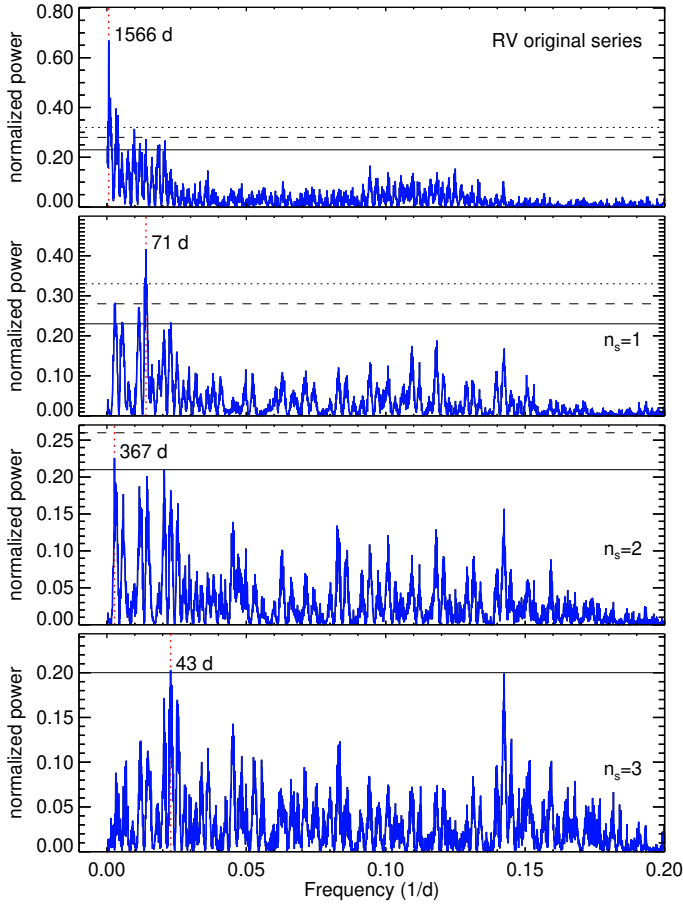
Fig. 5. Generalised Lomb-Scargle periodogram of the HARPS and HARPS-N data of BD-11 4672 (*top panel*) and the residuals obtained after removing the n_s−signals best-fit solution (*second to fourth panels*). In each panel, the periodogram's most significant frequency is identified by a vertical dotted red line and labeled by its corresponding period, while the horizontal solid, dashed and dotted lines respectively identify the 10, 1, and 0.1% FAP levels.

period $P_{\rm rot,max} = 30 \pm 15$ d, even if the large errorbars on the measurements of $v \sin i$ translate into large uncertainties on this estimates. Moreover, BD-11 4672 has not been observed by the Transiting Exoplanet Survey Satellite (TESS, Ricker et al. 2015) during its nominal mission. However, as the TESS extended mission is set to observe also in the ecliptic, it may help to obtain a photometric measurement of the rotation period of BD-11 4672 in the near future.

A common technique to estimate the value of the stellar rotation period is from the empirical relationships between stellar rotation and the mean activity level (e.g. Noyes et al. 1984; Mamajek & Hillenbrand 2008). The mean activity level is usually measured by means of the $\log R'_{\rm HK}$, which was defined for FGK-type stars by Noyes et al. (1984), but is not calibrated for lower-mass stars, as late-K and M dwarfs. Different calibration procedures have been proposed in recent years to compute the $\log R'_{\rm HK}$ for late-type stars, such as those by Astudillo-Defru et al. (2017a) and Suárez Mascareño et al. (2018). We used these two calibration procedures to derive the mean values of $\log R'_{\rm HK}$ from the S-index computed from our HARPS-N spectra, and obtained the similar values of $\log R'_{\rm HK} = -4.65$ and $\log R'_{\rm HK} = -4.71$ from Astudillo-Defru et al. (2017a) and Suárez Mascareño et al. (2018) respectively. These authors also provide activity-rotation relationships, from which we obtained estimates for BD-11 4672's

rotation period of $P_{\rm rot} = 24.7 \pm 2.5$ d and $P_{\rm rot} = 19.6 \pm 2$ d, respectively. The uncertainties are estimated from the dispersion of the activity-rotation relationship, which is on the order of ~10% (Astudillo-Defru et al. 2017a), and show that the two values are compatible within 2σ.

3.2. Orbital fitting of the radial velocities

After excluding from the radial velocity time series the four outliers discussed in Sect. 3.1, we have a total of 107 datapoints. 41 of those are archival HARPS measurements and 66 come from our HARPS-N monitoring of the star.

We started by investigating the main peak of the after prewhitening full time series GLS periodogram (see top panel of Fig. 5), located at 1566 d with a false alarm probability (FAP) of 0.01% as calculated via bootstrap method, in order to provide an updated orbital solution for the known planet b first reported in Moutou et al. (2015). We searched for the best fit orbital solution through a differential evolution Markov chain Monte Carlo method based on the EXOFAST suite (Eastman et al. 2013; Desidera et al. 2014). For a single-Keplerian, eccentric solution the nine free parameters were inferior conjunction epoch T_0, orbital period P, $\sqrt{e}\cos\omega$, $\sqrt{e}\sin\omega$, semi-amplitude K, and, for each instrument considered (HARPS and HARPS-N), a zeropoint radial velocity γ and an uncorrelated stellar jitter term j added in quadrature to the radial velocity measurement error. Uninformative priors were used for all parameters, explicitly setting minimum and maximum boundaries only for P and T_0 in order to better explore the parameter region most relevant to each analysed signal. Eighteen chains were run simultaneously and reached convergence and good mixing according to the criteria established in Eastman et al. (2013).

We find a single-Keplerian solution (see second column of Table 3) with semiamplitude $K_{\rm b} = 14.58^{+1.08}_{-1.04}$ m s^{-1}, period $P_{\rm b} = 1628 \pm 12$ d and eccentricity $e_{\rm b} = 0.10 \pm 0.06$, from which we derive minimum mass $M_{\rm b} \sin i = 0.63 \pm 0.05\ M_{\rm Jup}$ and semimajor axis $a_{\rm b} = 2.35 \pm 0.04$ au. We note that the Keplerian parameters of this solution are all comparable to those reported in Moutou et al. (2015) within 1σ. Due to the larger estimate of the stellar mass derived in Sect. 2, we obtain larger values of minimum mass and semi-major axis. Also, we note that the $e_{\rm b}$ values of both solutions are compatible with zero within 2σ.

The periodogram of the residuals to the single-planet solution (shown in the second panel of Fig. 5) features a significant peak at 71 d with FAP = 0.01% lacking any counterpart in the activity indices discussed in Sect. 3.1 and shown in Fig. 3, suggesting the presence of an additional planetary companion.

We find the best-fit two-Keplerian solution (see third column of Table 3) to have orbital periods, $P_{\rm b} = 1631 \pm 13$ d and $P_{\rm c} = 74.18^{+0.10}_{-0.12}$ d; semiamplitudes, $K_{\rm b} = 14.59^{+1.01}_{-0.98}$ m s^{-1} and $K_{\rm c} = 3.48^{+0.78}_{-0.67}$ m s^{-1}; and eccentricities, $e_{\rm b} = 0.08^{+0.06}_{-0.05}$ and $e_{\rm c} = 0.34^{+0.18}_{-0.17}$. For planet b, this solution implies minimum mass, $M_{\rm b} \sin i = 0.63 \pm 0.05\ M_{\rm Jup}$; and semimajor axis, $a_{\rm b} = 2.36 \pm 0.04$ au. Again, we note that $e_{\rm b}$ is compatible with zero within 2σ. In order to compare this two-planet solution with the singleplanet one that we found, we compute the Bayesian Information Criterion (BIC) values of each solution as:

$$\mathrm{BIC} = k \log n - 2 \log \mathscr{L}, \tag{1}$$

with k as the number of model parameters, n the datapoint number, and $\log \mathscr{L}$ the maximum log-likelihood computed by EXOFAST. We find this two-Keplerian solution to describe the time series significantly better than the single-planet one, having

Table 3. Adopted priors and results of the Markov chain Monte Carlo orbital fits.

Parameter	Priors	1 planet	2 planets	2 planets + year-long signal (adopted solution)
K_b (m s^{-1})	$\mathcal{U}(0, +\infty)$	$14.58^{+1.08}_{-1.04}$	$14.59^{+1.01}_{-0.98}$	$14.88^{+1.10}_{-1.22}$
P_b (d)	$\mathcal{U}(1000, 2000)$	1628 ± 12	1631 ± 13	1634^{+13}_{-14}
$\sqrt{e_b}\cos\omega_b$	$\mathcal{U}(-1, 1)$	$0.07^{+0.13}_{-0.15}$	$0.10^{+0.14}_{-0.17}$	$0.11^{+0.15}_{-0.18}$
$\sqrt{e_b}\sin\omega_b$	$\mathcal{U}(-1, 1)$	$-0.28^{+0.16}_{-0.10}$	$-0.20^{+0.17}_{-0.12}$	$-0.04^{+0.16}_{-0.14}$
$T_{0,b}$ (BJD-2450000)	$\mathcal{U}(6700, 8700)$	$7905.4^{+42.1}_{-49.0}$	$7908.6^{+41.9}_{-52.2}$	$7915.3^{+33.9}_{-48.3}$
e_b	Derived	0.10 ± 0.06	$0.08^{+0.06}_{-0.05}$	$0.05^{+0.05}_{-0.03}$
ω_b (deg)	Derived	$281.94^{+28.11}_{-36.57}$	$287.73^{+35.90}_{-78.12}$	$343.88^{+92.63}_{-66.95}$
$M_b \sin i$ (M_{Jup})	Derived	0.63 ± 0.05	0.63 ± 0.05	$0.65^{+0.05}_{-0.06}$
a_b (au)	Derived	2.35 ± 0.04	2.36 ± 0.04	2.36 ± 0.04
K_c (m s^{-1})	$\mathcal{U}(0, +\infty)$	–	$3.48^{+0.78}_{-0.67}$	$3.42^{+0.70}_{-0.64}$
P_c (d)	$\mathcal{U}(70, 80)$	–	$74.18^{+0.10}_{-0.12}$	$74.20^{+0.06}_{-0.08}$
$T_{0,c}$ (BJD-2 450 000)	$\mathcal{U}(8620, 8700)$	–	$8685.4^{+5.6}_{-5.9}$	$8687.5^{+5.66}_{-5.92}$
$\sqrt{e_c}\cos\omega_c$	$\mathcal{U}(-1, 1)$	–	$-0.14^{+0.28}_{-0.23}$	$-0.24^{+0.24}_{-0.20}$
$\sqrt{e_c}\sin\omega_c$	$\mathcal{U}(-1, 1)$	–	$-0.51^{+0.25}_{-0.16}$	$-0.54^{+0.21}_{-0.14}$
e_c	Derived	–	$0.34^{+0.18}_{-0.17}$	$0.40^{+0.13}_{-0.15}$
ω_c (deg)	Derived	–	$253.68^{+30.49}_{-33.98}$	$245.92^{+23.02}_{-26.58}$
$M_c \sin i$ ($M_\oplus$)	Derived	–	$16.59^{+3.14}_{-2.97}$	$15.37^{+2.97}_{-2.81}$
a_c (au)	Derived	–	0.30 ± 0.01	0.30 ± 0.01
K_{yr} (m s^{-1})	$\mathcal{U}(0, +\infty)$	–	–	$2.40^{+0.54}_{-0.52}$
P_{yr} (d)	$\mathcal{U}(200, 400)$	–	–	$365.46^{+5.96}_{-36.55}$
$T_{0,yr}$ (BJD-2450000)	$\mathcal{U}(8300, 8700)$	–	–	$8480.4^{+21.81}_{-20.01}$
γ_{HARPS} (m s^{-1})	$\mathcal{U}(-\infty, +\infty)$	$3.83^{+0.69}_{-0.64}$	3.96 ± 0.62	$3.83^{+0.87}_{-0.82}$
$\gamma_{HARPS-N}$ (m s^{-1})	$\mathcal{U}(-\infty, +\infty)$	$9.78^{+1.20}_{-1.23}$	$9.59^{+1.30}_{-1.27}$	$9.11^{+1.25}_{-1.33}$
Jitter$_{HARPS}$ (m s^{-1})	$\mathcal{U}(0, +\infty)$	$3.21^{+0.57}_{-0.47}$	$2.58^{+0.65}_{-0.48}$	$2.42^{+0.55}_{-0.47}$
Jitter$_{HARPS-N}$ (m s^{-1})	$\mathcal{U}(0, +\infty)$	$4.17^{+0.44}_{-0.38}$	$3.49^{+0.40}_{-0.37}$	$2.98^{+0.34}_{-0.30}$
Residuals rms (m s^{-1})		4.00	3.56	3.01
Maximum log $\mathcal{L}$		-199.39	-180.18	-167.35
BIC		440.83	425.78	414.13

Notes. The listed best fit values and uncertainties are the medians and 16th–84th percentiles of the posterior distributions, respectively.

respectively $BIC_{2pl} = 425.78$ and $BIC_{1pl} = 440.83$, the difference of $\Delta BIC = -15.05$ between the two solutions representing a strong evidence in favour of the two-Keplerian solution.

We therefore report the detection of a second planetary companion orbiting at 74 days around star BD-11 4672 and for which we derive minimum mass $M_c \sin i = 16.59^{+3.14}_{-2.97} M_\oplus$ and semimajor axis $a_c = 0.30 \pm 0.01$ au; in Figs. 6 and 7 we show, respectively, the orbital fit and the phase-folded curves for our proposed two-planet solution. We also note that this Neptune-mass planet orbits slightly outside the inner edge of the optimistic circumstellar habitable zone, located at 0.33 au.

As shown in the third panel of Fig. 5, the periodogram of the two-planet residuals features a low-significance peak with FAP = 5% at 367 d. This one-year residual peak is likely to be a spurious signal induced by the Earth's motion around the Sun, similarly to the annual signal first reported and characterised in Dumusque et al. (2015) using HARPS data, in which imperfections in the HARPS CCD can lead to a deformation of specific spectral lines passing by the crossing block stitching of the detector. A similar spurious signal has recently been detected in HARPS-N also, as reported in Benatti et al. (2020). As prescribed in Dumusque et al. (2015), the correction and removal of this low-significance signal is possible either by removing from the correlation mask the spectral lines affected by this effect or by fitting a sinusoidal with a one-year period to the radial velocity time series. While the first approach is beyond the scope of this paper and may prove more fruitful for follow-up studies of system BD-11 4672, the inclusion of an additional one-year sine signal to our radial velocity fit may help in provide a more complete and robust characterisation of the system.

We find the best fit three-signal model to feature eccentric solutions for planets b and c and a circular solution for the
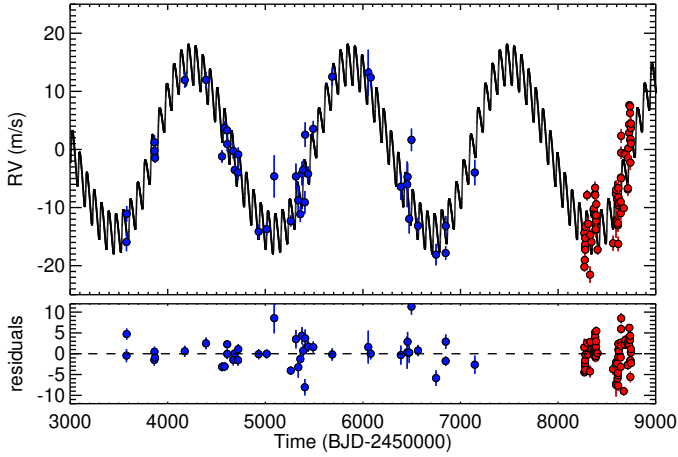
Fig. 6. Orbital fit for the two-planet solution of system BD-11 4672. *Top panel*: best-fit solution is shown as a black curve over the literature data points from HARPS (blue) and our HARPS-N observations (red). *Bottom panel*: residual radial velocities.
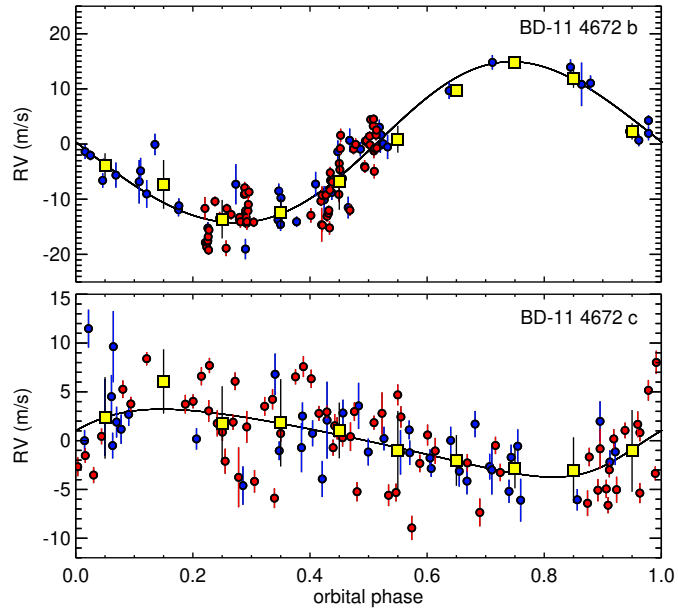

Fig. 8. Same as Fig. 6 for the two-planets solution including the year-long circular signal.

Fig. 7. Phase-folded radial velocity curves for our two-planets solution of the BD-11 4672 system. The best-fit solution for each planet is shown as a black curve over the literature data points from HARPS (blue) and our HARPS-N observations (red). The yellow squares and their error bars represent the binned averages and standard deviations of the measurements.
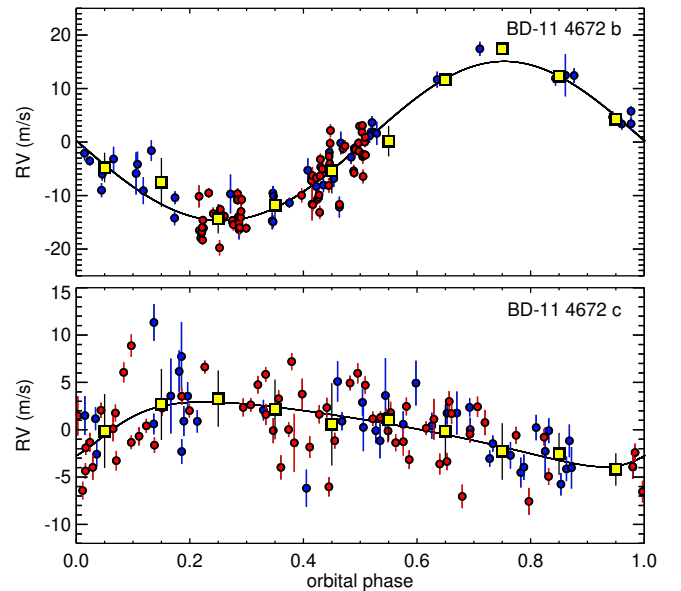
Fig. 9. Same as Fig. 7 for the two-planets solution including the year-long circular signal

third, yearly signal (see fourth column of Table 3 and Figs. 8 and 9). In this solution, we find planet b and c to have semi-amplitudes, $K_b = 14.88^{+1.10}_{-1.22}$ m s^{-1} and $K_c = 3.42^{+0.70}_{-0.64}$ m s^{-1}; orbital periods, $P_b = 1634^{+13}_{-14}$ d and $P_c = 74.20^{+0.06}_{-0.08}$ d; eccentricities, $e_b = 0.05^{+0.05}_{-0.03}$ and $e_c = 0.40^{+0.13}_{-0.15}$, from which we derive minimum masses, $M_b \sin i = 0.65^{+0.05}_{-0.06} M_{\rm Jup}$, $M_c \sin i = 15.37^{+2.97}_{-2.81} M_{\oplus}$; and semimajor axes, $a_b = 2.36 \pm 0.04$ au, $a_c = 0.30 \pm 0.01$ au. The circular Keplerian which we fit the year-long signal with has semiamplitude $K_{\rm yr} = 2.40^{+0.54}_{-0.52}$ m s^{-1} and period $P_c = 365.46^{+5.96}_{-36.55}$ d. The main peak in the three-signal residual periodogram (shown in the fourth panel of Fig. 5) has FAP = 11% and is found at 43 d, a period we identified in Sect. 3.1 as related to stellar rotation or activity, along with its alias peak at
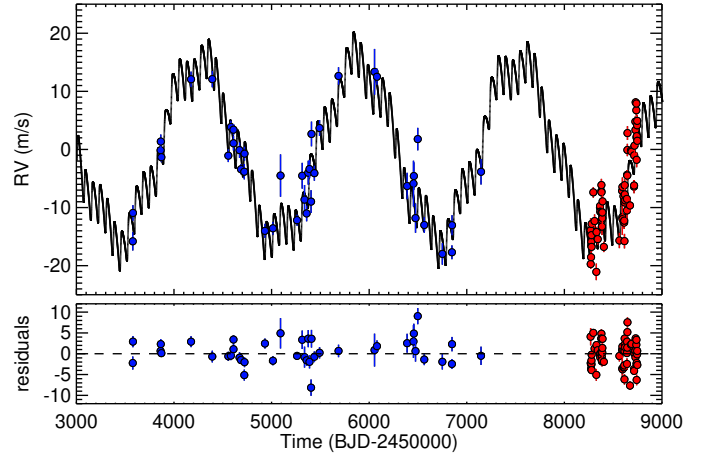
7 d. The low FAP of both peaks and the lack of convergence shown by the tentative four-signals fits we have run suggest that the available radial velocity time series do not currently hint at the presence of additional companions.

All orbital parameters for the two planets in the system are compatible with those returned by the two-Keplerian solution; additionally, with a BIC value of 414.13 and a ΔBIC = -11.65 it is clear that the three-signal solution is statistically favoured to the two-Keplerian solution detailed in the previous paragraphs. Finally, we note that the ΔBIC = -26.40 between this three-signal solution and the single-planet one represents a much stronger evidence in favour of the presence of planet c that the one provided by the ΔBIC = -15.05 between the two-Keplerian and single-planet solutions and we therefore adopt this orbital solution.

4. Dynamics

As discussed in Sect. 3.2, we detected the presence of the new Neptune-mass planet BD-11 4672 c, which, at semimajor axis
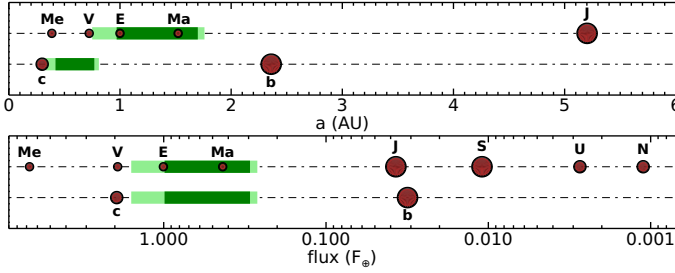
Fig. 10. Architecture of planetary system BD-11 4672 compared with that of the Solar System in semi-major axis (*top panel*) and incident flux scale (*bottom panel*). The conservative and optimistic habitable zones are shown as dark and light green bands, respectively.

$a_c = 0.30 \pm 0.01$ au, is located just outside of the inner edge of the optimistic circumstellar habitable zone that ranges from 0.33 to 0.81 au.

Figure 10 shows the architecture of the BD-11 4672 system as described by our three-signal solution and a comparison with the Solar System. It is interesting to note that planet b receives an incident flux $F_b = 0.03\,F_\oplus$, while planet c has an incident flux of $F_c = 1.95\,F_\oplus$ comparable to that of Venus. We note, however, that the stellar parameters and planetary masses of the BD-11 4672 system are very different from those of the aforementioned Solar System bodies and, therefore, the analogy between the two systems are only for the sake of comparing the incident fluxes of the planets involved.

It could be interesting to pursue the study of the dynamical evolution and long-term stability of possible lower-mass additional companions in the habitable zone of the system, especially to gauge the dynamical effect of the presence of the newly detected eccentric Neptune-mass planet located just outside the inner edge of the habitable zone. While a full and detailed analysis of dynamical stability of the system lies beyond the scope of this paper, a preliminary and accurate approach to the problem is represented by the angular momentum deficit (AMD) stability criterion presented and detailed in Laskar (2000); Laskar & Petit (2017); Petit et al. (2018).

With this method, a *n*-body planetary system is considered to be AMD-stable if its angular momentum deficit, defined as the difference between the norm of the angular momentum of the system and that of a coplanar and circular system having the same semimajor axes a_k:

$$C = \sum_{k=1}^{n} M_k \sqrt{GM_\star a_k}\left(1 - \sqrt{1 - e_k^2}\cos i_k\right),\tag{2}$$

is not sufficient to allow for planetary collisions. In particular, a pair of planets in which the inner one has mass M, semimajor axis a and eccentricity e and the outer one has M', a', e' is considered AMD-stable if:

$$\beta = \frac{\mathscr{C}}{C_{cr}} < 1,\tag{3}$$

with $\mathscr{C}$ the relative AMD defined as:

$$\mathscr{C} = \gamma\sqrt{\alpha}\left(1 - \sqrt{1 - e^2}\right) + \left(1 - \sqrt{1 - e'^2}\right),\tag{4}$$

having denoted $\gamma = M/M'$ and $\alpha = a/a'$, and C_{cr} is the critical AMD similarly computed for the pair of critical eccentricities

e_{cr}, e'_{cr} that satisfy the collision conditions:

$$\alpha e_{cr} + e'_{cr} - 1 + \alpha = 0$$
$$\alpha e_{cr} + \frac{\gamma e_{cr}}{\sqrt{\alpha\left(1 - e_{cr}^2\right) + \gamma^2 e_{cr}^2}} = 0.\tag{5}$$

For multiplanetary systems, the whole system is considered AMD-stable if for every adjacent pair of planets the condition $\beta < 1$ is satisfied. While it is important to note that the AMD stability criterion is unable to take into account mean motion resonances and secular chaotic interactions that can further promote or impede the dynamical stability as observed in our own Solar System (Laskar 2008; Laskar & Gastineau 2009; Batygin et al. 2015), the AMD stability criterion provides a useful test for assessing the long-term stability of planetary systems and has recently been fruitfully used to characterise the dynamical stability of exoplanetary systems. It has also often been found to be in agreement with Hill stability criterion and dynamical simulations (e.g. Zinzi & Turrini 2017; Agnew et al. 2018; Petit et al. 2018; Stock et al. 2020).

As a first test on the AMD-stability of the BD-11 4672 system, we calculated the β of the pair composed by planets b and c as characterised by our best fit orbital solution and assuming coplanarity; in order to also account for the uncertainties on relevant quantities $a_{b,c}$, $M_{b,c}$ and $e_{b,c}$, we performed the AMD-stability test for 10^4 random values of said quantities uniformly drawn within their best fit errorbars reported in Sect. 3.2 and listed in the fourth column of Table 3. We find the range of values for $\beta_{b,c}$ between 0.002 to 0.027, proving the long-term stability of our proposed two-planet solution. This is in agreement with a dynamical simulation we have performed with the MERCURY *N*-body integrator package (Chambers 1999) using astrocentric input coordinates and the hybrid symplectic/Bulirsch-Stoer integrator with a one-day initial timestep, also showing that the best fit two-planet configuration is stable up to 10 Myr, as would also be expected by computing the Hill radii of the planets as:

$$R_H = a(1 - e)\sqrt[3]{\frac{M_p}{3M_\star}}\tag{6}$$

and obtaining $R_{H,b} = 0.146$ au and $R_{H,c} = 0.005$ au, from which it is evident that planets b and c are separated by many mutual Hill radii.

In order to assess the long-term dynamical stability of possible additional planets orbiting within the habitable zone of the system and, especially, its dependence on the presence of planet c near its inner edge having a significant eccentricity of $e_c = 0.40^{+0.13}_{-0.15}$, we inject a single additional planet having dynamical mass M_{inj} between 1 and 15 $M_\oplus$, eccentricity e_{inj} between 0 and 0.5 and semimajor axis a_{inj} between the inner and outer boundary of the optimistic habitable zone (0.33–0.81 au). Assuming coplanarity for all bodies in the system, we calculate the $\beta_{b,inj}$ and $\beta_{c,inj}$ for each injection, again making 10^4 random draws of the a, M and e of known planets b and c within their best fit uncertainties for each realisation of (M_{inj}, a_{inj}). Following Laskar & Petit (2017), the three-planet system is considered AMD-stable if and only if both $\beta_{b,inj}$ and $\beta_{c,inj}$ are below 1.

In Fig. 11, we show the results of the AMD stability tests we performed on a 50×50 (M_{inj}, a_{inj}) grid, the colour scale representing the fraction of AMD-stable three-planet systems obtained from the 10^4 random draws of $a_{b,c}$, $M_{b,c}$ and $e_{b,c}$. As a first point, we must note that the more massive and distant planet b has no impact on the AMD-stability of the habitable zone by
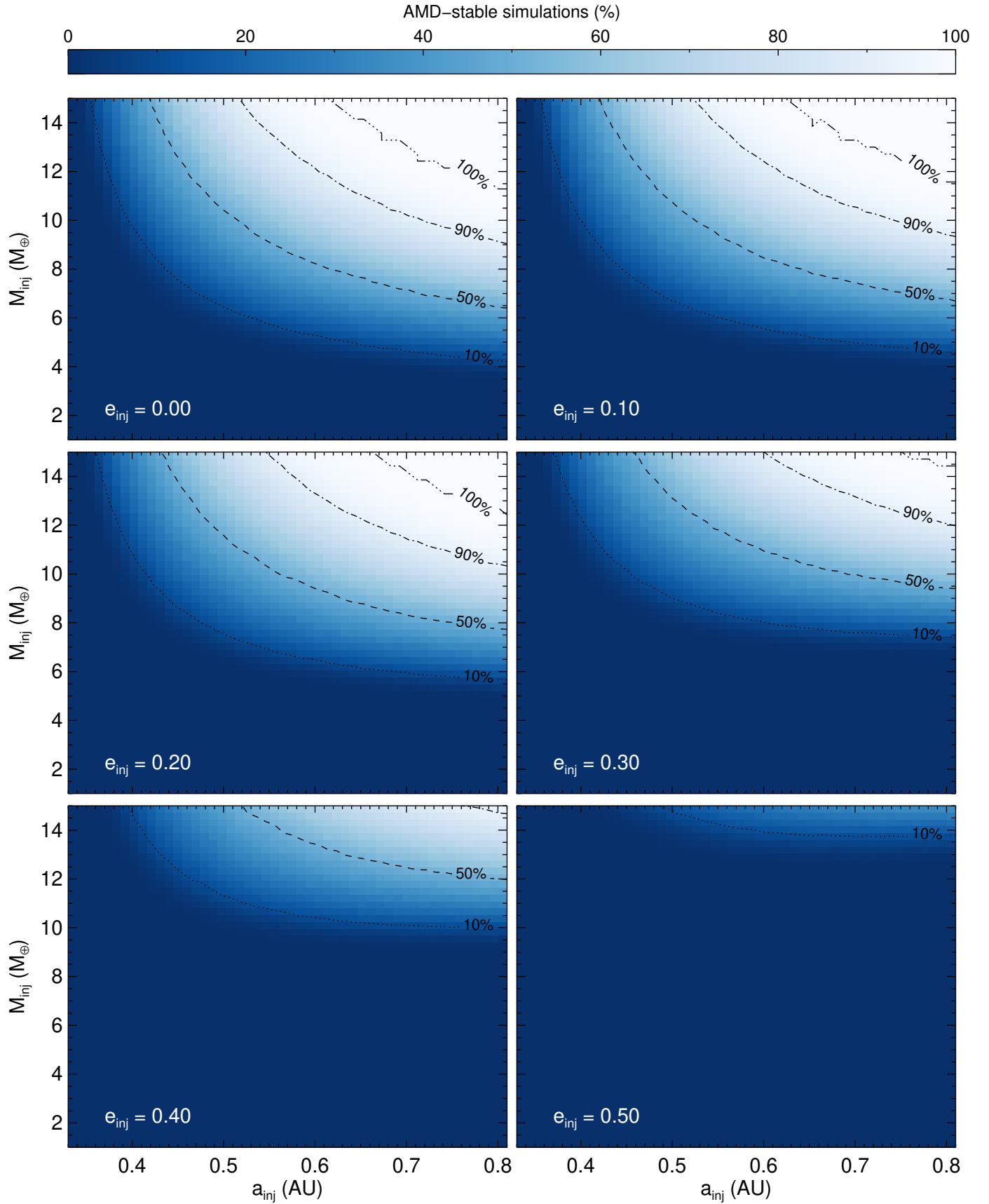
Fig. 11. Results of the AMD-stability tests made for the two-planets solution of system BD-11 4672 and injecting a single additional planet in the circumstellar habitable zone, colour-coded according to the fraction of AMD-stable three-planets systems obtained for each injection and 10^4 random draws of the a, M, and e of known planets b and c within their best-fit uncertainties.

virtue of its near-zero eccentricity, as every configuration tested returned $\beta_{b,inj} < 1$; as could be expected from its proximity and eccentricity, planet c represents the main influence on the stability of the habitable zone of the system, significantly disrupting the stability of neighbouring planetary bodies.

Indeed, almost every injection of additional planets with $a_{inj} < 0.4$ au is found to result in an AMD-unstable system regardless of its e_{inj} and M_{inj}, with less than 30% of the simulations being AMD-stable only in the $e_{inj} < 0.3$ and $M_{inj} > 10\,M_\oplus$ cases; the more eccentric the additional planet is, the less AMD-stable the three-planet system grows, finally resulting in a fully AMD-unstable habitable zone for $e_{inj} > 0.40$. Ultimately, AMD-stability appears to be possible for more than 90% of the simulated systems only in the case of Neptune-mass ($M_{inj} \geq 10$) planets orbiting on relatively low-eccentric ($e_{inj} \leq 0.30$) orbits in the outer portion ($a_{inj} > 0.5$ au) of the habitable zone. Barring resonances and secular interaction that can stabilise an AMD-unstable system or vice versa (Zinzi & Turrini 2017; Agnew et al. 2018; Petit et al. 2018; Stock et al. 2020) that are not yet considered by the AMD stability test, we therefore expect yet-undetected temperate Neptune-mass planetary bodies, if any, to be present in the BD-11 4672 system only on low- to moderate-eccentricity orbits on the outer region of the circumstellar habitable zone.

5. Discussion and conclusions

In the present work, we report the results of the high-precision monitoring of the K-dwarf BD-11 4672 conducted with HARPS-N within the GAPS programme from May 2018 to September 2019, performed to search for additional subgiant planetary companions to the already known giant planet BD-11 4672 b that was first detected by Moutou et al. (2015).

We provide a new characterisation of the physical properties of the host star, finding larger values of mass and radius than those reported in the literature; we also characterise the star as a metal-poor member of the thin-disc stellar population. Additionally, it may be noted that BD-11 4672 appears to be among the most α-poor thin-disc stars at similar [Fe/H]. This makes this K-dwarf a possibly interesting counter-example to previous works (e.g. Haywood 2008, 2009; Kang et al. 2011; Adibekyan et al. 2012b,c; Maldonado et al. 2018) that noted a tendency for metal-poor planet-hosting stars to feature an overabundance of α-elements, possibly promoting the core-accretion formation of gas giant planets by compensating for low [Fe/H]. By studying the stellar activity of BD-11 4672 we find three dominant periodicities in the activity indices Ca II H&K, Hα, and Na I D_1 D_2 at ~3000, ~200 and ~40 days. Finally, combining the newly derived projected rotational velocity value of $v \sin i = 1 \pm 0.5\,\mathrm{km\,s^{-1}}$, and the empirical relations between stellar rotation and mean activity level, we provide an estimate of rotation period of $P_{rot} \sim 25$ days.

The densely sampled time series obtained with HARPS-N allowed us, in conjunction with literature HARPS radial velocity measurements, to provide an updated orbital solution to known planet BD-11 4672 b. Our orbital solution is compatible and better constrained than the one of the discovery paper (Moutou et al. 2015), although it is interesting to note that our solution features slightly larger values of minimum mass and semimajor axis for the planet, mainly stemming from the larger stellar mass we obtained from our spectroscopic characterisation of the host star. In addition to this, we report the detection of new planet BD-11 4672 c, which has an orbital period of $74.20^{+0.06}_{-0.08}$ days, eccentricity of $0.40^{+0.13}_{-0.15}$, and radial velocity
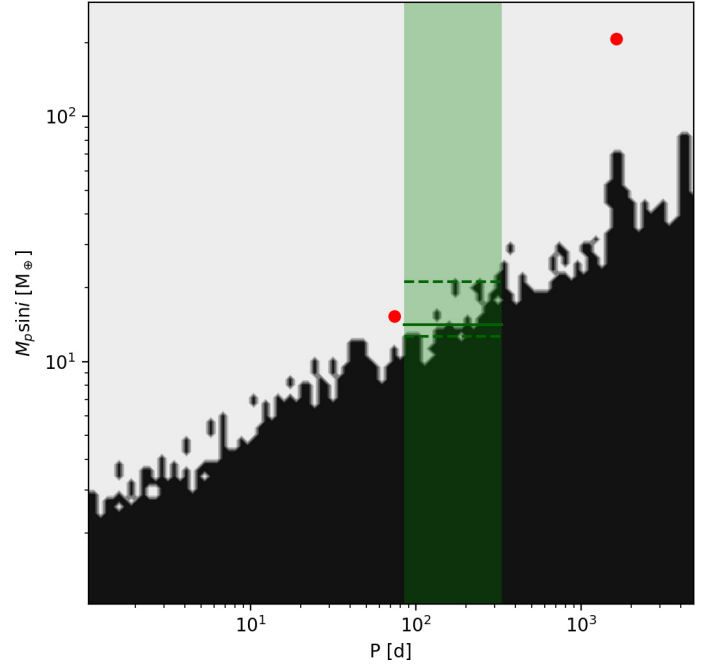

Fig. 12. Detection map for the complete RV time series of BD-114672. The white part corresponds to the area in the period – minimum mass space where additional signals could be detected if present in the data, while the black region corresponds to the area where the detection probability is negligible. The red circles mark the position in the parameter space of the two planets in the system. The green areas denote the circumstellar habitable zone and the horizontal green lines mark the corresponding median detection threshold (solid line), with its 16–84% uncertainties (dashed lines).

semiamplitude of $3.42^{+0.70}_{-0.64}\,\mathrm{m\,s^{-1}}$, for which we derive minimum mass of $15.37^{+2.97}_{-2.81}\,M_\oplus$ and semimajor axis of 0.30 ± 0.01 au. Receiving an incident flux of $1.95\,F_\oplus$, we note that this Neptune-mass planet is found on a slightly more inner location than the optimistic circumstellar habitable zone. We also note that in the historical HARPS time series a low-significance peak is present around 71 d with a high FAP = 52% in the single-planet residuals; it is therefore clear that the inclusion of our high-cadence HARPS-N data is instrumental in confirming and identifying this residual peak.

To investigate the effects that Neptune-mass planet c would have on the dynamical stability of additional temperate low-mass planets by virtue of its eccentricity and proximity to the inner edge of the habitable zone of the system, we have conducted AMD stability tests to evaluate the long-term stability of the system with the injection of additional planetary bodies with $M_{inj} = 1-15\,M_\oplus$ and $e_{inj} = 0-0.5$ orbiting within the habitable zone. In doing so, we find that planet c has a severely negative effect on the region of parameters space in which the injection of an additional planet keeps the system AMD-stable, only allowing the long-term stability of the more massive, distant and less eccentric injected temperate bodies.

We computed the detection threshold for the HARPS-N dataset following the Bayesian approach from Tuomi et al. (2014). We applied this technique on the combined RV time series, including in the model the three signals identified in Sect. 3.2. The 2D-map of the detection function is shown in Fig. 12: focussing on the circumstellar habitable zone as studied in our dynamical analysis in Sect. 4, we obtain a minimum-mass detection threshold of $14.19^{+6.96}_{-1.53}\,M_\oplus$. Thus, it would be possible

Table 4. Proper motions for BD-11 4672 and their variations from a linear mean motions as retrieved from the Hipparcos-*Gaia* Catalog of Accelerations (Brandt 2018, 2019).

	Hipparcos	*Gaia* DR2
μ_α (mas yr^{-1})	-286.814 ± 1.862	-288.590 ± 0.156
μ_δ (mas yr^{-1})	-237.047 ± 1.419	-235.560 ± 0.145
$\Delta\mu_\alpha$ (mas yr^{-1})	1.466 ± 1.863	-0.309 ± 0.169
$\Delta\mu_\delta$ (mas yr^{-1})	-1.528 ± 1.420	-0.042 ± 0.153

for a low-eccentricity super-Earth to remain undetected in our data, inside the AMD-stable orbital region shown in Fig. 11.

Another source of information that could potentially be useful for the characterisation of the BD-11 4672 planetary system comes from the use of astrometric measurements, especially from future data releases of the *Gaia* mission. Indeed, using the relation

$$\alpha = \frac{M_p}{M_\star} \frac{a}{d}, \tag{7}$$

we can provide an estimate of the astrometric signature α produced by each planet in the system and evaluate which astrometric contribution could be in principle detected at high S/N ($\alpha \gtrsim 50\,\mu\text{as}$), using the nominal minimum mass obtained from our best fit solutions to provide a lower estimate of α. While the astrometric signature $\alpha_c \sim 0.8\,\mu\text{as}$ of Neptune-mass planet c is clearly too low to be detected by *Gaia*, we find giant planet b to have $\alpha_b \sim 83\,\mu\text{as}$, a value suggesting the possibility of a future astrometric characterisation of the planet's orbit.

Additionally, the use of variations in the proper motions measurements of BD-11 4672 between the Hipparcos (ESA 1997) and *Gaia* DR2 epochs can provide a useful element in estimating a preliminary constraint on the true mass of planet b. In Table 4, we list the variations, $\Delta\mu_{\alpha,\delta}$, from a purely linear stellar mean motion for BD-11 4672 as reported in the Hipparcos-*Gaia* Catalog of Accelerations (HGCA, Brandt 2018, 2019), in which the Hipparcos and *Gaia* catalogues have been cross-calibrated to account for systematics and shift all proper motions in the DR2 reference frame; it is also worth noting that the HGCA uncertainties on *Gaia* DR2 proper motions are larger than those reported in the DR2 catalogue and listed in Table 2 as a result of the different model of error inflation used in Brandt (2018, 2019).

Over the ~ 24 yr between the Hipparcos and *Gaia* measurements, BD-11 4672 has deviated very little from a purely linear motion in the plane of the sky; the variation between the two measurement epochs being comparable to zero within $\sim 1\sigma$. If we assume that the entirety of this low deviation is due to the orbital motion of the outer giant planet b, we can compute the expected variations in proper motions $\Delta\mu$ that would be caused by different orbital inclinations i_b and, therefore, true mass M_b, starting at our best fit nominal value of minimum mass, $M_b \sin i_b = 0.65\,M_{\text{Jup}}$, and finding the critical orbital inclination and, therefore, maximum true mass that would cause a proper motion variation equal to that reported in Brandt (2018, 2019). Using the traditional expressions for astrometric motions in the Thiele-Innes element representation (Makarov & Kaplan 2005; Sozzetti et al. 2014), we find that any true mass for planet b above $\sim 1.98\,M_{\text{Jup}}$ would produce astrometric accelerations higher than those reported in Brandt (2018, 2019), therefore constraining the true mass of planet b well below the brown dwarf traditional limit of $\sim 13\,M_{\text{Jup}}$. This maximum value for M_b corresponds to

orbital inclination of $i_b > 19°$; additionally assuming a coplanar configuration for the BD-11 4672 planetary system, this critical inclination would in turn imply a maximum mass of $M_c \sim 47\,M_\oplus$ for planet c, therefore constraining its true mass to be at most about 2.7 times the mass of Neptune.

The BD-11 4672 system is worthy of additional monitoring and study to better characterise its interesting system architecture and investigate its dynamical origins. With an eccentricity of $0.40^{+0.13}_{-0.15}$, planet BD-11 4672 c is notable for being among the most eccentric Neptune-mass exoplanets found at intermediate orbital period. Indeed, it has been noted from both known transiting and radial velocity detected exoplanetary populations (Halbwachs et al. 2005; Ribas & Miralda-Escudé 2007; Brahm et al. 2019; Correia et al. 2020) that Neptune-mass or -sized exoplanets with P between 50 and 100 d are typically found on lower eccentricities, with notable exceptions, such as GJ 96 b (Hobson et al. 2018) and Kepler-278 c (Van Eylen & Albrecht 2015) that may hint at some shared eccentricity excitation mechanisms. Additionally, while the different stellar and planetary masses do not allow for a proper consideration of the BD-11 4672 system as a scaled-down Solar System analogue, we note again that planets b and c receive a stellar flux similar to that received by Jupiter and Venus respectively, possibly hinting at some shared dynamical history. It is also worth noting that the BD-11 4672 system architecture, with a long-period giant planet and one inner lower-mass planet, is an example of the planetary architecture some of the authors of this paper searched for around 20 solar-type stars as detailed in Barbato et al. (2018).

The BD-11 4672 system joins a small, but growing, group of Doppler-detected exoplanetary systems around K and M dwarfs showing a clear mass hierarchy, with outer more massive companions and inner lower-mass planets, such as GJ 676 A (Anglada-Escudé & Tuomi 2012) and GJ 221 (Lo Curto et al. 2013). While such sub-solar dwarfs are noted in the literature to have a lower probability of hosting long-period giant planets than Sun-like stars and, rather, are usually host to various super-Earths, the presence of such an architecture around BD-11 4672 could be taken as a positive sign with regard to the variety of planetary systems that formation and migration mechanisms are capable of producing among a large range of stellar types.

References

Adibekyan, V. Z., Sousa, S. G., Santos, N. C., et al. 2012a, A&A, 545, A32
Adibekyan, V. Z., Santos, N. C., Sousa, S. G., et al. 2012b, A&A, 543, A89
Adibekyan, V. Z., Delgado Mena, E., Sousa, S. G., et al. 2012c, A&A, 547, A36
Agnew, M. T., Maddison, S. T., & Horner, J. 2018, MNRAS, 481, 4680
Anglada-Escudé, G., & Butler, R. P. 2012, ApJS, 200, 15
Anglada-Escudé, G., & Tuomi, M. 2012, A&A, 548, A58

Astudillo-Defru, N., Delfosse, X., Bonfils, X., et al. 2017a, A&A, 600, A13
Astudillo-Defru, N., Forveille, T., Bonfils, X., et al. 2017b, A&A, 602, A88
Barbato, D., Sozzetti, A., Desidera, S., et al. 2018, A&A, 615, A175
Barbato, D., Sozzetti, A., Biazzo, K., et al. 2019, A&A, 621, A110
Batygin, K., Morbidelli, A., & Holman, M. J. 2015, ApJ, 799, 120
Benatti, S., Damasso, M., Desidera, S., et al. 2020, A&A, 639, A50
Bensby, T., Feltzing, S., & Lundström, I. 2003, A&A, 410, 527
Bensby, T., Feltzing, S., Lundström, I., & Ilyin, I. 2005, A&A, 433, 185
Biazzo, K., Gratton, R., Desidera, S., et al. 2015, A&A, 583, A135
Bitsch, B., Lambrechts, M., & Johansen, A. 2015, A&A, 582, A112
Bonfils, X., Gillon, M., Udry, S., et al. 2012, A&A, 546, A27
Bonfils, X., Delfosse, X., Udry, S., et al. 2013, A&A, 549, A109
Boro Saikia, S., Marvin, C. J., Jeffers, S. V., et al. 2018, A&A, 616, A108
Brahm, R., Espinoza, N., Rabus, M., et al. 2019, MNRAS, 483, 1970
Brandt, T. D. 2018, ApJS, 239, 31
Brandt, T. D. 2019, ApJS, 241, 39
Butler, R. P., Vogt, S. S., Marcy, G. W., et al. 2004, ApJ, 617, 580
Castelli, F., & Kurucz, R. L. 2004, IAU Symp., 210, A20
Chabrier, G., & Baraffe, I. 2000, ARA&A, 38, 337
Chambers, J. E. 1999, MNRAS, 304, 793
Choi, J., Dotter, A., Conroy, C., et al. 2016, ApJ, 823, 102
Correia, A. C. M., Bourrier, V., & Delisle, J. B. 2020, A&A, 635, A37
Cosentino, R., Lovis, C., Pepe, F., et al. 2012, Proc. SPIE, 8446, 84461V
Cossou, C., Raymond, S. N., Hersant, F., & Pierens, A. 2014, A&A, 569, A56
Covino, E., Esposito, M., Barbieri, M., et al. 2013, A&A, 554, A28
Crossfield, I. J. M., Petigura, E., Schlieder, J. E., et al. 2015, ApJ, 804, 10
Cutri, R. M., Skrutskie, M. F., van Dyk, S., et al. 2003, VizieR Online Data Catalog: II/246
Damasso, M., Biazzo, K., Bonomo, A. S., et al. 2015, A&A, 575, A111
Desidera, S., Sozzetti, A., Bonomo, A. S., et al. 2013, A&A, 554, A29
Desidera, S., Bonomo, A. S., Claudi, R. U., et al. 2014, A&A, 567, L6
Dotter, A. 2016, ApJS, 222, 8
Dressing, C. D., & Charbonneau, D. 2013, ApJ, 767, 95
Dumusque, X., Pepe, F., Lovis, C., & Latham, D. W. 2015, ApJ, 808, 171
Eastman, J., Gaudi, B. S., & Agol, E. 2013, PASP, 125, 83
Eastman, J. D., Rodriguez, J. E., Agol, E., et al. 2019, PASP, submitted, [arXiv:1907.09480]
ESA 1997, The Hipparcos and Tycho Catalogues, ESA SP, 1200
Forveille, T., Bonfils, X., Lo Curto, G., et al. 2011, A&A, 526, A141
Gaia Collaboration (Brown, A. G. A., et al.) 2018, A&A, 616, A1
Gomes da Silva, J., Santos, N. C., Bonfils, X., et al. 2011, A&A, 534, A30
Halbwachs, J. L., Mayor, M., & Udry, S. 2005, A&A, 431, 1129
Haywood, M. 2008, A&A, 482, 673
Haywood, M. 2009, ApJ, 698, L1
Hobson, M. J., & Gomez, M. 2017, New Aston., 55, 1
Hobson, M. J., Díaz, R. F., Delfosse, X., et al. 2018, A&A, 618, A103
Høg, E., Fabricius, C., Makarov, V. V., et al. 2000, A&A, 355, L27
Izidoro, A., Raymond, S. N., Morbidelli, A., Hersant, F., & Pierens, A. 2015a, ApJ, 800, L22
Izidoro, A., Morbidelli, A., Raymond, S. N., Hersant, F., & Pierens, A. 2015b, A&A, 582, A99
Johnson, J. A., Butler, R. P., Marcy, G. W., et al. 2007, ApJ, 670, 833
Johnson, J. A., Aller, K. M., Howard, A. W., & Crepp, J. R. 2010, PASP, 122, 905
Kang, W., Lee, S.-G., & Kim, K.-M. 2011, ApJ, 736, 87
Kopparapu, R. K., Ramirez, R., Kasting, J. F., et al. 2013, ApJ, 765, 131
Kopparapu, R. K., Ramirez, R. M., SchottelKotte, J., et al. 2014, ApJ, 787, L29
Lambrechts, M., Morbidelli, A., Jacobson, S. A., et al. 2019, A&A, 627, A83
Laskar, J. 2000, Phys. Rev. Lett., 84, 3240
Laskar, J. 2008, Icarus, 196, 1
Laskar, J., & Gastineau, M. 2009, Nature, 459, 817
Laskar, J., & Petit, A. C. 2017, A&A, 605, A72
Laughlin, G., Bodenheimer, P., & Adams, F. C. 2004, ApJ, 612, L73
Lo Curto, G., Mayor, M., Benz, W., et al. 2013, A&A, 551, A59
Lo Curto, G., Pepe, F., Avila, G., et al. 2015, The Messenger, 162, 9
Lovis, C., & Pepe, F. 2007, A&A, 468, 1115
Makarov, V. V., & Kaplan, G. H. 2005, AJ, 129, 2420
Maldonado, J., Villaver, E., & Eiroa, C. 2018, A&A, 612, A93
Mamajek, E. E., & Hillenbrand, L. A. 2008, ApJ, 687, 1264
Mayor, M., Pepe, F., Queloz, D., et al. 2003, The Messenger, 114, 20
Morbidelli, A., & Raymond, S. N. 2016, J. Geophys. Res. Planets, 121, 1962
Mordasini, C., Alibert, Y., & Benz, W. 2009a, A&A, 501, 1139
Mordasini, C., Alibert, Y., Benz, W., & Naef, D. 2009b, A&A, 501, 1161
Moutou, C., Mayor, M., Lo Curto, G., et al. 2011, A&A, 527, A63
Moutou, C., Lo Curto, G., Mayor, M., et al. 2015, A&A, 576, A48
Noyes, R. W., Hartmann, L. W., Baliunas, S. L., Duncan, D. K., & Vaughan, A. H. 1984, ApJ, 279, 763

Petit, A. C., Laskar, J., & Boué, G. 2018, A&A, 617, A93
Pinamonti, M., Damasso, M., Marzari, F., et al. 2018, A&A, 617, A104
Pojmanski, G. 1997, Acta Astron., 47, 467
Raymond, S. N., Barnes, R., & Mandell, A. M. 2008, MNRAS, 384, 663
Ribas, I., & Miralda-Escudé, J. 2007, A&A, 464, 779
Ricker, G. R., Winn, J. N., Vanderspek, R., et al. 2015, J. Astron. Telesc. Instrum. Syst., 1, 014003
Scandariato, G., Maldonado, J., Affer, L., et al. 2017, A&A, 598, A28
Schlaufman, K. C. 2014, ApJ, 790, 91
Skiff, B. A. 2014, VizieR Online Data Catalog: B/mk, 1, 2023
Sneden, C. 1973, ApJ, 184, 839
Soubiran, C., & Girard, P. 2005, A&A, 438, 139
Sozzetti, A., Giacobbe, P., Lattanzi, M. G., et al. 2014, MNRAS, 437, 497
Stassun, K. G., & Torres, G. 2018, ApJ, 862, 61
Stock, S., Kemmer, J., Reffert, S., et al. 2020, A&A, 636, A119
Suárez Mascareño, A., Rebolo, R., González Hernández, J. I., et al. 2018, A&A, 612, A89
Tody, D. 1993, ASP Conf. Ser., 52, 173
Trifonov, T., Tal-Or, L., Zechmeister, M., et al. 2020, A&A, 636, A74
Tuomi, M., Jones, H. R. A., Barnes, J. R., Anglada-Escudé, G., & Jenkins, J. S. 2014, MNRAS, 441, 1545
Valenti, J. A., & Fischer, D. A. 2005, ApJS, 159, 141
Van Eylen, V., & Albrecht, S. 2015, ApJ, 808, 126
Winn, J. N., & Fabrycky, D. C. 2015, ARA&A, 53, 409
Winters, J. G., Henry, T. J., Lurie, J. C., et al. 2015, AJ, 149, 5
Wittenmyer, R. A., Butler, R. P., Horner, J., et al. 2020a, MNRAS, 491, 5248
Wittenmyer, R. A., Wang, S., Horner, J., et al. 2020b, MNRAS, 492, 377
Zacharias, N., Finch, C. T., Girard, T. M., et al. 2012, VizieR Online Data Catalog: I/322A
Zechmeister, M., & Kürster, M. 2009, A&A, 496, 577
Zhu, W., & Wu, Y. 2018, AJ, 156, 92
Zinzi, A., & Turrini, D. 2017, A&A, 605, L4

[1] Dipartimento di Fisica, Università degli Studi di Torino, Via Pietro Giuria 1, 10125 Torino, Italy

[2] INAF – Osservatorio Astrofisico di Torino, Via Osservatorio 20, 10025 Pino Torinese, Italy
e-mail: domenico.barbato@inaf.it

[3] Observatoire de Genève, Université de Genève, 51 Chemin des Maillettes, 1290 Sauverny, Switzerland

[4] INAF – Osservatorio Astrofisico di Catania, Via S. Sofia 78, 95123 Catania, Italy

[5] INAF – Osservatorio Astronomico di Roma, Via Frascati 33, 00078 Monte Porzio Catone, Italy

[6] INAF – Osservatorio Astronomico di Palermo, Piazza del Parlamento 1, 90134 Palermo, Italy

[7] INAF – Osservatorio Astronomico di Padova, Vicolo dell'Osservatorio 5, 35122 Padova, Italy

[8] Dipartimento di Fisica, Università di Roma Tor Vergata, Via della Ricerca Scientifica 1, 00133 Roma, Italy

[9] Max Planck Institute for Astronomy, Königstuhl 17, 69117 Heidelberg, Germany

[10] Fundación Galileo Galilei - INAF, Rambla José Ana Fernandez Pérez 7, 38712 Breña Baja, TF, Spain

[11] INAF – Osservatorio Astronomico di Trieste, Via Tiepolo 11, 34143 Trieste, Italy

[12] INAF – Osservatorio Astronomico di Brera, Via E. Bianchi 46, 23807 Merate (LC), Italy

[13] Astronomy Department and Van Vleck Observatory, Wesleyan University, Middletown, CT 06459, USA

[14] INAF – Osservatorio Astronomico di Capodimonte, Salita Moiariello 16, 80131 Napoli, Italy

[15] Instituto de Astrofísica de Canarias, C/Vía Láctea s/n, 38205 La Laguna, Spain

[16] INAF – Osservatorio Astronomico di Cagliari, Via della Scienza 5, 09047 Selargius (CA), Italy

[17] Dipartimento di Fisica e Astronomia "G. Galilei", Università di Padova, Vicolo dell'Osservatorio 3, 35122 Padova, Italy

[18] INAF – Osservatorio Astrofisico di Arcetri, Largo E. Fermi 5, 50125 Firenze, Italy

Appendix A: Additional tables

Table A.1. HARPS measurements for BD-11 4672.

BJD	T_{exp} (s)	RV (m s^{-1})	BIS (km s^{-1})	*FWHM* (km s^{-1})	Ca II	Hα	Na I
2 453 577.64	450	−11.98 ± 1.58	0.0456	6.1098	0.0362 ± 0.0007	0.0488 ± 0.0002	0.00380 ± 0.00005
2 453 579.64	450	−7.10 ± 1.34	0.0278	6.0924	0.0374 ± 0.0006	0.0489 ± 0.0002	0.00373 ± 0.00004
2 453 862.82	509	3.69 ± 1.38	0.0420	6.1024	0.0351 ± 0.0006	0.0485 ± 0.0002	0.00381 ± 0.00004
2 453 864.81	450	5.19 ± 1.21	0.0320	6.0971	0.0362 ± 0.0006	0.0484 ± 0.0002	0.00372 ± 0.00004
2 453 870.79	890	2.49 ± 0.86	0.0392	6.0923	0.0334 ± 0.0004	0.0483 ± 0.0001	0.00371 ± 0.00003
2 454 174.90	450	15.91 ± 1.32	0.0269	6.0897	0.0350 ± 0.0006	0.0482 ± 0.0002	0.00364 ± 0.00003
2 454 392.50	450	15.94 ± 1.40	0.0339	6.0764	0.0307 ± 0.0005	0.0485 ± 0.0002	0.00370 ± 0.00004
2 454 556.89	450	2.76 ± 1.10	0.0392	6.0695	0.0295 ± 0.0004	0.0480 ± 0.0001	0.00366 ± 0.00003
2 454 582.83	663	7.69 ± 1.09	0.0297	6.0841	0.0318 ± 0.0005	0.0481 ± 0.0001	0.00366 ± 0.00003
2 454 609.77	541	7.24 ± 0.97	0.0303	6.0803	0.0323 ± 0.0004	0.0491 ± 0.0001	0.00368 ± 0.00003
2 454 609.84	541	4.89 ± 1.25	0.0310	6.0852	0.0323 ± 0.0005	0.0490 ± 0.0001	0.00369 ± 0.00003
2 454 671.71	900	3.71 ± 1.33	0.0322	6.0640	0.0289 ± 0.0005	0.0484 ± 0.0002	0.00362 ± 0.00003
2 454 686.59	676	0.43 ± 0.89	0.0317	6.0803	0.0299 ± 0.0004	0.0482 ± 0.0001	0.00367 ± 0.00003
2 454 720.56	667	0.00 ± 1.32	0.0312	6.0705	0.0305 ± 0.0005	0.0483 ± 0.0002	0.00364 ± 0.00003
2 454 722.60	900	3.10 ± 1.19	0.0379	6.0778	0.0291 ± 0.0005	0.0483 ± 0.0001	0.00370 ± 0.00003
2 454 931.90	450	−10.18 ± 1.21	0.0381	6.0770	0.0301 ± 0.0005	0.0488 ± 0.0001	0.00367 ± 0.00003
2 455 013.71	900	−9.74 ± 1.10	0.0407	6.1003	0.0326 ± 0.0006	0.0483 ± 0.0002	0.00371 ± 0.00004
2 455 091.54	450	−0.67 ± 3.64	0.0315	6.1237	0.0418 ± 0.0014	0.0489 ± 0.0003	0.00364 ± 0.00007
2 455 260.90	900	−8.35 ± 0.96	0.0408	6.1089	0.0367 ± 0.0005	0.0494 ± 0.0001	0.00373 ± 0.00003
2 455 313.83	900	−0.69 ± 2.22	0.0378	6.1264	0.0345 ± 0.0009	0.0496 ± 0.0002	0.00379 ± 0.00005
2 455 337.90	500	−4.80 ± 2.51	0.0382	6.1337	0.0324 ± 0.0010	0.0491 ± 0.0002	0.00371 ± 0.00005
2 455 358.87	900	−7.18 ± 1.36	0.0418	6.1345	0.0355 ± 0.0007	0.0494 ± 0.0002	0.00381 ± 0.00004
2 455 375.72	450	−0.17 ± 2.05	0.0273	6.1303	0.0350 ± 0.0009	0.0495 ± 0.0002	0.00385 ± 0.00005
2 455 388.65	450	0.46 ± 1.58	0.0290	6.1349	0.0345 ± 0.0007	0.0490 ± 0.0002	0.00379 ± 0.00004
2 455 404.66	450	−5.14 ± 1.97	0.0310	6.1218	0.0367 ± 0.0009	0.0491 ± 0.0002	0.00381 ± 0.00005
2 455 408.73	900	6.50 ± 2.12	0.0224	6.1333	0.0375 ± 0.0009	0.0489 ± 0.0002	0.00379 ± 0.00005
2 455 438.63	450	−0.26 ± 1.29	0.0360	6.1075	0.0329 ± 0.0006	0.0489 ± 0.0002	0.00377 ± 0.00003
2 455 491.51	676	7.51 ± 1.37	0.0319	6.1142	0.0366 ± 0.0007	0.0487 ± 0.0002	0.00386 ± 0.00004
2 455 685.94	450	16.47 ± 1.50	0.0404	6.1450	0.0377 ± 0.0007	0.0491 ± 0.0002	0.00385 ± 0.00004
2 456 023.85	900	12.65 ± 1.30	0.0332	6.1211	0.0471 ± 0.0007	0.0520 ± 0.0001	0.00381 ± 0.00003
2 456 023.89	600	11.89 ± 1.45	0.0428	6.1238	0.0420 ± 0.0008	0.0511 ± 0.0002	0.00381 ± 0.00004
2 456 054.76	448	17.18 ± 3.95	0.0494	6.1539	0.0383 ± 0.0014	0.0497 ± 0.0003	0.00381 ± 0.00008
2 456 079.79	600	16.34 ± 1.39	0.0380	6.1206	0.0355 ± 0.0007	0.0492 ± 0.0002	0.00378 ± 0.00004
2 456 388.92	415	−2.46 ± 2.28	0.0410	6.1057	0.0370 ± 0.0009	0.0486 ± 0.0002	0.00369 ± 0.00005
2 456 453.80	800	−2.05 ± 3.94	0.0298	6.1220	0.0313 ± 0.0014	0.0485 ± 0.0003	0.00364 ± 0.00008
2 456 457.79	450	−0.75 ± 2.36	0.0409	6.1212	0.0352 ± 0.0009	0.0484 ± 0.0002	0.00384 ± 0.00005
2 456 474.67	450	−7.99 ± 2.51	0.0563	6.1177	0.0321 ± 0.0012	0.0483 ± 0.0003	0.00378 ± 0.00007
2 456 497.76	900	5.61 ± 1.94	0.0283	6.1255	0.0402 ± 0.0009	0.0479 ± 0.0002	0.00395 ± 0.00005
2 456 564.48	538	−9.17 ± 1.35	0.0270	6.0805	0.0280 ± 0.0006	0.0484 ± 0.0002	0.00365 ± 0.00003
2 456 749.90	500	−14.14 ± 1.85	0.0450	6.0983	0.0345 ± 0.0009	0.0484 ± 0.0002	0.00367 ± 0.00005
2 456 847.73	900	−13.87 ± 1.19	0.0298	6.0915	0.0296 ± 0.0006	0.0477 ± 0.0002	0.00382 ± 0.00003
2 456 848.83	900	−9.21 ± 1.73	0.0322	6.1045	0.0309 ± 0.0007	0.0480 ± 0.0002	0.00381 ± 0.00004
2 457 145.91	600	−0.01 ± 2.20	0.0228	6.0728	0.0267 ± 0.0010	0.0479 ± 0.0003	0.00371 ± 0.00006

Table A.2. HARPS-N measurements for BD-11 4672.

BJD	T_{exp} (s)	RV (m s^{-1})	BIS (km s^{-1})	*FWHM* (km s^{-1})	Ca II	Hα	Na I
2 458 268.63	1200	−4.81 ± 2.08	0.0349	6.1400	0.0314 ± 0.0008	0.0485 ± 0.0002	0.00397 ± 0.00005
2 458 269.64	1200	−10.61 ± 0.83	0.0464	6.1334	0.0324 ± 0.0003	0.0487 ± 0.0001	0.00384 ± 0.00002
2 458 270.69	1200	−9.78 ± 1.66	0.0569	6.1282	0.0286 ± 0.0005	0.0491 ± 0.0002	0.00428 ± 0.00004
2 458 273.67	1200	−9.43 ± 1.03	0.0451	6.1359	0.0324 ± 0.0004	0.0486 ± 0.0001	0.00372 ± 0.00002
2 458 275.62	900	−7.45 ± 0.72	0.0424	6.1409	0.0320 ± 0.0003	0.0487 ± 0.0001	0.00380 ± 0.00002
2 458 276.64	1200	−6.77 ± 0.98	0.0480	6.1413	0.0325 ± 0.0004	0.0487 ± 0.0001	0.00379 ± 0.00003

Table A.2. continued.

BJD	T_{exp} (s)	RV (m s^{-1})	BIS (km s^{-1})	$FWHM$ (km s^{-1})	Ca II	Hα	Na I
2 458 277.59	1200	−5.65 ± 0.74	0.0440	6.1462	0.0334 ± 0.0003	0.0486 ± 0.0001	0.00384 ± 0.00002
2 458 278.65	1200	−7.66 ± 0.83	0.0468	6.1462	0.0323 ± 0.0003	0.0486 ± 0.0001	0.00381 ± 0.00002
2 458 279.66	1200	−3.71 ± 0.81	0.0478	6.1477	0.0321 ± 0.0003	0.0486 ± 0.0001	0.00390 ± 0.00002
2 458 296.57	1200	1.73 ± 0.91	0.0530	6.1740	0.0367 ± 0.0004	0.0489 ± 0.0001	0.00376 ± 0.00002
2 458 309.50	1200	−3.21 ± 1.15	0.0498	6.1509	0.0312 ± 0.0004	0.0491 ± 0.0002	0.00390 ± 0.00003
2 458 327.57	1200	−11.96 ± 1.43	0.0443	6.1526	0.0324 ± 0.0007	0.0491 ± 0.0002	0.00385 ± 0.00004
2 458 329.55	1200	−5.10 ± 0.89	0.0461	6.1581	0.0336 ± 0.0004	0.0488 ± 0.0001	0.00376 ± 0.00002
2 458 341.43	1200	−6.33 ± 0.95	0.0465	6.1591	0.0350 ± 0.0004	0.0490 ± 0.0001	0.00364 ± 0.00002
2 458 361.38	1200	−4.01 ± 2.10	0.0543	6.1667	0.0447 ± 0.0009	0.0517 ± 0.0002	0.00383 ± 0.00005
2 458 364.45	1200	−0.92 ± 0.95	0.0507	6.1623	0.0351 ± 0.0004	0.0492 ± 0.0002	0.00394 ± 0.00003
2 458 365.43	1200	−0.62 ± 0.72	0.0506	6.1619	0.0354 ± 0.0003	0.0490 ± 0.0001	0.00393 ± 0.00002
2 458 367.41	1200	−1.60 ± 1.11	0.0420	6.1579	0.0342 ± 0.0005	0.0496 ± 0.0002	0.00387 ± 0.00003
2 458 378.40	1200	1.94 ± 0.78	0.0445	6.1646	0.0363 ± 0.0004	0.0490 ± 0.0001	0.00381 ± 0.00002
2 458 379.40	1200	2.99 ± 1.07	0.0474	6.1706	0.0358 ± 0.0004	0.0489 ± 0.0001	0.00393 ± 0.00003
2 458 380.39	1200	1.75 ± 0.94	0.0482	6.1631	0.0368 ± 0.0004	0.0491 ± 0.0001	0.00374 ± 0.00002
2 458 381.37	1200	−1.79 ± 0.77	0.0428	6.1665	0.0363 ± 0.0004	0.0491 ± 0.0001	0.00376 ± 0.00002
2 458 382.38	1200	−1.64 ± 0.67	0.0478	6.1657	0.0367 ± 0.0003	0.0493 ± 0.0001	0.00380 ± 0.00002
2 458 383.36	1200	−3.05 ± 1.19	0.0480	6.1650	0.0357 ± 0.0006	0.0491 ± 0.0002	0.00379 ± 0.00003
2 458 384.36	1200	−4.27 ± 0.91	0.0485	6.1588	0.0362 ± 0.0004	0.0488 ± 0.0001	0.00374 ± 0.00003
2 458 385.36	1200	−4.15 ± 1.46	0.0480	6.1576	0.0338 ± 0.0006	0.0490 ± 0.0002	0.00384 ± 0.00004
2 458 388.35	1200	−2.70 ± 0.72	0.0434	6.1537	0.0358 ± 0.0003	0.0487 ± 0.0001	0.00375 ± 0.00002
2 458 389.36	1200	−1.73 ± 2.15	0.0532	6.1567	0.0336 ± 0.0008	0.0489 ± 0.0002	0.00369 ± 0.00005
2 458 391.35	1200	0.17 ± 1.08	0.0430	6.1557	0.0364 ± 0.0004	0.0490 ± 0.0001	0.00373 ± 0.00002
2 458 404.34	1200	−7.66 ± 0.89	0.0496	6.1607	0.0345 ± 0.0004	0.0493 ± 0.0001	0.00386 ± 0.00002
2 458 563.75	1200	−6.56 ± 1.31	0.0467	6.1450	0.0345 ± 0.0006	0.0491 ± 0.0002	0.00378 ± 0.00004
2 458 591.67	1200	1.98 ± 0.90	0.0489	6.1710	0.0364 ± 0.0005	0.0492 ± 0.0001	0.00381 ± 0.00003
2 458 593.72	900	−2.55 ± 3.06	0.0491	6.1708	0.0387 ± 0.0010	0.0492 ± 0.0002	0.00381 ± 0.00005
2 458 594.76	900	2.66 ± 1.63	0.0504	6.1744	0.0305 ± 0.0004	0.0493 ± 0.0002	0.00404 ± 0.00003
2 458 595.74	900	−2.87 ± 1.15	0.0521	6.1652	0.0357 ± 0.0005	0.0491 ± 0.0001	0.00383 ± 0.00003
2 458 605.70	1200	1.06 ± 0.83	0.0473	6.1617	0.0368 ± 0.0004	0.0491 ± 0.0001	0.00384 ± 0.00002
2 458 608.73	1200	−3.30 ± 0.99	0.0463	6.1598	0.0350 ± 0.0004	0.0488 ± 0.0001	0.00391 ± 0.00003
2 458 612.72	1200	−3.47 ± 1.11	0.0509	6.1653	0.0365 ± 0.0005	0.0489 ± 0.0001	0.00390 ± 0.00003
2 458 613.66	1200	−3.14 ± 0.91	0.0558	6.1616	0.0378 ± 0.0004	0.0492 ± 0.0001	0.00370 ± 0.00002
2 458 615.66	900	−6.66 ± 1.25	0.0514	6.1590	0.0355 ± 0.0005	0.0488 ± 0.0001	0.00382 ± 0.00003
2 458 616.68	900	0.00 ± 0.90	0.0498	6.1599	0.0368 ± 0.0004	0.0491 ± 0.0001	0.00374 ± 0.00002
2 458 617.66	900	2.96 ± 1.07	0.0447	6.1570	0.0361 ± 0.0005	0.0486 ± 0.0001	0.00377 ± 0.00003
2 458 618.63	900	1.37 ± 1.33	0.0468	6.1538	0.0351 ± 0.0006	0.0489 ± 0.0002	0.00384 ± 0.00003
2 458 622.70	1200	0.36 ± 0.90	0.0408	6.1731	0.0365 ± 0.0004	0.0488 ± 0.0001	0.00382 ± 0.00002
2 458 640.68	1200	0.60 ± 0.77	0.0473	6.1608	0.0372 ± 0.0004	0.0487 ± 0.0001	0.00372 ± 0.00002
2 458 641.60	1200	−1.39 ± 1.33	0.0471	6.1577	0.0377 ± 0.0006	0.0485 ± 0.0001	0.00373 ± 0.00003
2 458 642.67	1200	4.75 ± 0.80	0.0470	6.1644	0.0370 ± 0.0004	0.0485 ± 0.0001	0.00383 ± 0.00002
2 458 644.56	1200	4.63 ± 0.90	0.0462	6.1681	0.0356 ± 0.0005	0.0485 ± 0.0001	0.00381 ± 0.00003
2 458 645.64	1200	9.02 ± 1.06	0.0458	6.1633	0.0376 ± 0.0005	0.0486 ± 0.0001	0.00379 ± 0.00003
2 458 646.64	1200	11.93 ± 1.19	0.0480	6.1773	0.0379 ± 0.0005	0.0487 ± 0.0001	0.00379 ± 0.00003
2 458 672.44	1200	−0.53 ± 1.02	0.0512	6.1471	0.0331 ± 0.0005	0.0486 ± 0.0002	0.00387 ± 0.00003
2 458 682.57	1200	8.93 ± 0.95	0.0457	6.1585	0.0373 ± 0.0004	0.0486 ± 0.0001	0.00384 ± 0.00002
2 458 688.46	1200	8.73 ± 1.10	0.0515	6.1752	0.0384 ± 0.0004	0.0485 ± 0.0001	0.00392 ± 0.00003
2 458 713.42	1200	2.71 ± 1.14	0.0442	6.1488	0.0357 ± 0.0006	0.0492 ± 0.0001	0.00376 ± 0.00003
2 458 714.47	1200	2.91 ± 0.94	0.0441	6.1473	0.0341 ± 0.0004	0.0491 ± 0.0001	0.00382 ± 0.00003
2 458 715.43	1200	8.09 ± 1.00	0.0441	6.1489	0.0342 ± 0.0004	0.0487 ± 0.0001	0.00375 ± 0.00003
2 458 718.46	1200	9.77 ± 1.32	0.0407	6.1623	0.0362 ± 0.0006	0.0492 ± 0.0001	0.00374 ± 0.00003
2 458 727.42	1200	13.90 ± 0.90	0.0492	6.1843	0.0400 ± 0.0004	0.0499 ± 0.0001	0.00400 ± 0.00003
2 458 728.43	1200	12.46 ± 0.73	0.0570	6.1869	0.0386 ± 0.0003	0.0493 ± 0.0001	0.00393 ± 0.00002
2 458 730.43	1200	17.22 ± 0.69	0.0511	6.1883	0.0377 ± 0.0004	0.0493 ± 0.0001	0.00401 ± 0.00002
2 458 737.37	1200	15.85 ± 0.93	0.0458	6.1993	0.0402 ± 0.0004	0.0499 ± 0.0001	0.00382 ± 0.00002
2 458 738.38	1200	17.02 ± 0.78	0.0519	6.1928	0.0391 ± 0.0003	0.0496 ± 0.0001	0.00392 ± 0.00002
2 458 739.37	1200	11.15 ± 1.33	0.0427	6.1979	0.0389 ± 0.0006	0.0494 ± 0.0002	0.00378 ± 0.00003
2 458 740.37	1200	7.33 ± 1.28	0.0548	6.1962	0.0390 ± 0.0006	0.0494 ± 0.0002	0.00379 ± 0.00004
2 458 741.38	1200	11.39 ± 0.79	0.0552	6.1899	0.0395 ± 0.0004	0.0497 ± 0.0001	0.00396 ± 0.00002
2 458 745.38	1071	13.27 ± 0.96	0.0505	6.1780	0.0385 ± 0.0005	0.0489 ± 0.0001	0.00371 ± 0.00002
2 458 746.38	1200	14.04 ± 1.04	0.0488	6.1650	0.0382 ± 0.0005	0.0491 ± 0.0001	0.00385 ± 0.00003
2 458 747.41	1101	10.60 ± 0.84	0.0519	6.1652	0.0375 ± 0.0004	0.0489 ± 0.0001	0.00380 ± 0.00002